J|A|C|S
A R T I C L E S

$Xe_3OF_3^+$, a Precursor to a Noble-Gas Nitrate; Syntheses and Structural Characterizations of $FXeONO_2$, $XeF_2{\cdot}HNO_3$, and $XeF_2{\cdot}N_2O_4$

Matthew D. Moran, David S. Brock, Hélène P. A. Mercier, and Gary J. Schrobilgen*

Department of Chemistry, McMaster University, Hamilton, Ontario L8S 4M1, Canada

Received June 26, 2010; E-mail: schrobil@mcmaster.ca

Abstract: Xenon fluoride nitrate has been synthesized by reaction of NO_2F with $[FXeOXeFXeF][AsF_6]$ at −50 °C. It was characterized in SO_2ClF and CH_3CN solutions by low-temperature ^{14}N, ^{19}F, and ^{129}Xe NMR spectroscopy and in the solid state by low-temperature Raman spectroscopy (−160 °C) and single-crystal X-ray diffraction (−173 °C). The reactions were carried out using natural abundance and ^{18}O-enriched $[FXeOXeFXeF][AsF_6]$ and $^{15}NO_2F$ to aid in the vibrational assignments of $FXeONO_2$ and to establish the likely reaction pathway. Raman spectroscopy showed that $FXe^{16}ON(^{16}O^{18}O)$ was formed, along with XeF_2 and $[NO_2][AsF_6]$, when an excess of $N^{16}O_2F$ reacted with $[FXe^{18}OXeFXeF][AsF_6]$. A reaction mechanism consistent with these findings is discussed. The crystal structure consists of well-separated $FXeONO_2$ molecules which display no significant intermolecular interactions, providing geometric parameters that are in good agreement with the gas-phase values determined from quantum-chemical calculations. Decomposition of solid $FXeONO_2$ is proposed to occur by three reaction pathways to give XeF_2, Xe, O_2, N_2O_5, N_2O_4, and NO_2F. Attempts to synthesize $FXeONO_2$ and $Xe(ONO_2)_2$ by reaction of XeF_2 with HNO_3 in SO_2ClF solution below −30 °C led to $XeF_2{\cdot}HNO_3$. The structure of $XeF_2{\cdot}HNO_3$ includes a hydrogen bond between HNO_3 and a fluorine atom of XeF_2, as well as an interaction between the xenon atom and an oxygen atom of HNO_3, leading to a crystal lattice comprised of layered sheets. A molecular addition compound between XeF_2 and N_2O_4 crystallized from liquid N_2O_4 below 0 °C. The crystal structure of $XeF_2{\cdot}N_2O_4$ displayed weak interactions between the xenon atom of XeF_2 and the oxygen atoms of N_2O_4. Quantum-chemical calculations have been used to assign the vibrational spectra of $FXeONO_2$, $XeF_2{\cdot}HNO_3$, and $XeF_2{\cdot}N_2O_4$ and to better understand the nature of the interactions of HNO_3 and N_2O_4 with XeF_2. The synthesis of $[XeONO_2][AsF_6]$ was attempted by the reaction of $FXeONO_2$ with excess liquid AsF_5 between −78 and −50 °C, but resulted in slow formation of $[NO_2][AsF_6]$, Xe, and O_2. Thermodynamic calculations show that the pathways to $[XeONO_2][AsF_6]$ formation and decomposition are exothermic and spontaneous under standard conditions and at −78 °C.

1. Introduction

The greatest variety of polyatomic ligand groups bonded to xenon occurs for xenon in the +2 oxidation state, and those bonded through oxygen are the most prevalent. Neutral mono- and disubstituted oxygen-bonded derivatives having the formulations FXeL and/or XeL_2 have been reported where L = $OC(O)CF_3$,[1] $OP(O)F_2$,[2] OSO_2CF_3,[3] OSO_2F,[4,5] $OClO_3$,[5] $OSeF_5$,[6] $OTeF_5$,[7,8] and $OIOF_4$.[9] With the exception of $OP(O)F_2$[2] and $OIOF_4$,[9] their syntheses have been accomplished by reaction of the parent acid, HL, with XeF_2 according to eq 1 ($n = 1, 2$), leading to HF formation, a significant thermodynamic driving force in these reactions. Alternative syntheses of the $OSeF_5$[10] and $OTeF_5$[11,12] derivatives also exist which do not involve HF displacement.

$$XeF_2 + n\mathrm{HL} \rightarrow F_{2-n}XeL_n + n\mathrm{HF} \qquad (1)$$

Two prior studies have reported the formation of xenon(II) nitrates by HF displacement. The earlier study reports the reactions of XeF_2 with anhydrous HNO_3 containing 20% NO_2 by weight at 20 °C.[13] Red-brown solids were obtained that rapidly decomposed at 23 °C, forming an intense, transient blue color. It is likely that the blue color arose from N_2O_3.[14] The formulations $FXeONO_2$ and $Xe(ONO_2)_2$ were suggested, but no structural characterizations were provided. When these

---

(1) Musher, J. I. *J. Am. Chem. Soc.* **1968**, *90*, 7371–7372.
(2) Eisenberg, M.; DesMarteau, D. D. *Inorg. Chem.* **1972**, *11*, 1901–1904.
(3) Naumann, D.; Tyrra, W.; Gnann, R.; Pfolk, D. *J. Chem. Soc., Chem. Commun.* **1994**, 2651–2653.
(4) Bartlett, N.; Wechsberg, M.; Jones, G. R.; Burbank, R. D. *Inorg. Chem.* **1972**, *11*, 1124–1127.
(5) Wechsberg, M.; Bulliner, P. A.; Sladky, F. O.; Mews, R.; Bartlett, N. *Inorg. Chem.* **1972**, *11*, 3063–3070.
(6) Seppelt, K.; Nothe, D. *Inorg. Chem.* **1973**, *12*, 2727–2730.
(7) Sladky, F. O. *Monatsh. Chem.* **1970**, *101*, 1559–1570.
(8) Sladky, F. O. *Monatsh. Chem.* **1970**, *101*, 1571–1577.
(9) Syvret, R. G.; Schrobilgen, G. J. *Inorg. Chem.* **1989**, *28*, 1564–1573.
(10) Seppelt, K.; Lentz, D. *Inorg. Synth.* **1986**, *24*, 27–31.
(11) Schumacher, G. A.; Schrobilgen, G. J. *Inorg. Chem.* **1984**, *23*, 2923–2929.
(12) Jacob, E.; Lentz, D.; Seppelt, K. *Z. Anorg. Allg. Chem.* **1981**, *472*, 7–25.
(13) Eisenberg, M.; DesMarteau, D. D. *Inorg. Nucl. Chem. Lett.* **1970**, *6*, 29–34.
(14) Beattie, I. R. *Prog. Inorg. Chem.* **1963**, *5*, 1–26.

10.1021/ja105618w

Scheme 1. Proposed Pathway for the Reaction of $FXe^{18}OXeFXeF^+$ with NO_2F

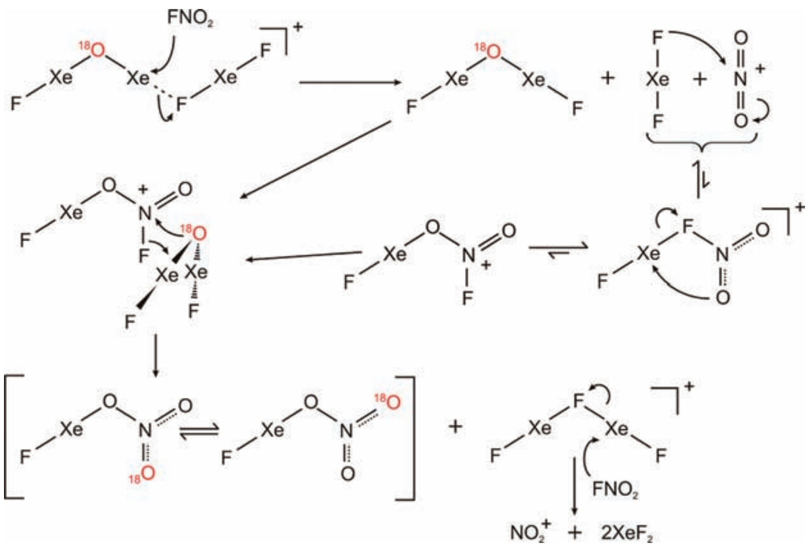

reactions were carried out at −20 °C, the red-brown solids were not observed. In a subsequent study, $FXeONO_2$ was reported to have been generated by the reaction of XeF_2 with HNO_3 in CH_2Cl_2 at −30 °C, and it was, in turn, reacted in situ with various alkenes to give 1,2-disubstituted fluoro-nitrato alkanes (1 = F, 2 = ONO_2).[15] The proposed intermediate xenon compound was not characterized in solution, nor was its isolation attempted.

The absence of a well-characterized xenon(II) nitrate is surprising because the nitrate anion meets the general criteria that are normally associated with a ligand that is suitable for stabilization of Xe in its +2 oxidation state: (1) the least electronegative atom of the ligand (nitrogen) is in its highest oxidation state, (2) NO_3^- is the conjugate base of a strong monoprotic acid, and correspondingly, (3) the electronegativity of the $-ONO_2$ ligand group is high. Empirical correlations based on the ^1H chemical shift difference between the α- and β-^1H resonances of CH_3CH_2X derivatives have been previously used to assign group electronegativities[16] based on the halogen electronegativities of Huggins.[17] This approach has been employed here using Pauling electronegativities[18] to give a group electronegativity for ONO_2 of 3.95,[16] which is close to those of fluorine (3.98)[18] and $OTeF_5$ (3.87).[19]

Recent work has shown that XeF_2 and $[H_3O][AsF_6]$ react in anhydrous HF to form the only known oxide fluoride cation of Xe(II), $[FXeOXeFXeF][AsF_6]$.[20] The present paper details the synthesis of $FXeONO_2$ from the $FXeOXeFXeF^+$ cation, providing an application of this interesting cation to the synthesis of a novel xenon compound. The decomposition of $FXeONO_2$, the attempted synthesis of $XeONO_2^+$, and the syntheses and structural characterizations of the molecular adduct, $XeF_2 \cdot HNO_3$, and the molecular addition compound, $XeF_2 \cdot N_2O_4$, are also described.

2. Results and Discussion

2.1. Synthesis and Decomposition of $FXeONO_2$. Deep red-orange to magenta $[FXeOXeFXeF][AsF_6]$[20] was allowed to react as a suspension with liquid NO_2F at −50 °C. A suspension of white solid formed over a 5 h period. Removal of excess NO_2F under vacuum at −110 °C yielded a white, powdered mixture of $FXeONO_2$, XeF_2, and $[NO_2][AsF_6]$. The reaction also proceeded to completion at −78 °C but required reaction times of 2−3 weeks. The latter method proved useful in establishing the proposed reaction pathway (Scheme 1). The solid changed in color from deep magenta to yellow-orange after 24−48 h, and finally to white. The yellow-orange color and resulting Raman spectrum of the intermediate reaction mixture showed the presence of a transient xenon oxide fluoride that is proposed to be $O(XeF)_2$ in Scheme 1. The latter compound will be the subject of a future publication. The proposed intermediates, $FXeON(O)F^+$ and $FXeFNO_2^+$, were shown to be stable species with all frequencies real, where the $FXeFNO_2^+$ isomer is ca. 80−90 kJ mol^{-1} more stable than $FXeON(O)F^+$ (Table S1 and Figure S1, Supporting Information). Moreover, $FXeON(O)F^+$ is also plausible in view of the existence of the structurally related $XN(O)F^+$ cations (X = N_3,[21] Cl,[22] CF_3,[22] and F[23]). The reaction pathway was also supported by an ^{18}O-enrichment and Raman spectroscopic study which showed that only $FXe^{16}ON(^{16}O^{18}O)$ was formed when $[FXe^{18}OXeFXeF][AsF_6]$ was used as the starting material. Failure to observe $FXe^{18}ONO_2$ indicated that no oxygen isotope scrambling had occurred among the bridging ^{16}O and terminal ^{18}O atoms (see Raman Spectroscopy). A weak Raman band was observed at 1362 cm^{-1} in the ^{18}O-enriched spectrum of the $FXe^{16}ON(^{16}O^{18}O)/[NO_2][AsF_6]$ product mixture. The band is attributed to the mixed $^{18}ON^{16}O^+$ cation which results from a minor exchange pathway (Scheme 2; see Raman Spectroscopy).

The polar-covalent compounds, $FXeONO_2$ and XeF_2, were separated from $[NO_2][AsF_6]$ and the decomposition products, N_2O_4 and N_2O_5, by rapidly extracting $FXeONO_2/XeF_2$ into SO_2ClF at −30 °C, followed by decanting the supernatant from

---

(15) Zefirov, N. S.; Gakh, A. A.; Zhdankin, V. V.; Stang, P. J. *J. Org. Chem.* **1991**, *56*, 1416–1418.

(16) Dailey, B. P.; Shoolery, J. N. *J. Am. Chem. Soc.* **1955**, *77*, 3977–3981.

(17) Huggins, M. L. *J. Am. Chem. Soc.* **1953**, *75*, 4123–4126.

(18) Allred, A. L. *J. Inorg. Nucl. Chem.* **1961**, *17*, 215–221.

(19) Birchall, T.; Myers, R. D.; de Waard, H.; Schrobilgen, G. J. *Inorg. Chem.* **1982**, *21*, 1068–1073.

(20) Gerken, M.; Moran, M. D.; Mercier, H. P. A.; Pointner, B. E.; Schrobilgen, G. J.; Hoge, B.; Christe, K. O.; Boatz, J. A. *J. Am. Chem. Soc.* **2009**, *131*, 13474–13489.

(21) Wilson, W. W.; Haiges, R.; Boatz, J. A.; Christe, K. O. *Angew. Chem., Int. Ed.* **2007**, *46*, 3023–3027.

(22) Minkwitz, R.; Bernstein, D.; Preut, H.; Sartori, P. *Inorg. Chem.* **1991**, *30*, 2157–2161.

(23) Vij, A.; Zhang, X.; Christe, K. O. *Inorg. Chem.* **2001**, *40*, 416–417.

Scheme 2. Proposed Pathway for the Formation of the $^{18}ON^{16}O^+$ Cation

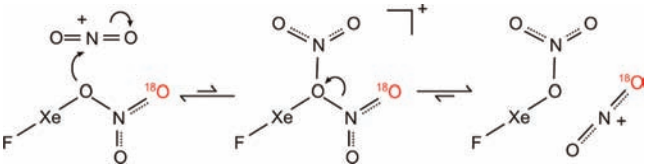

solid [NO$_2$][AsF$_6$], N$_2$O$_4$, and N$_2$O$_5$. A mixture of FXeONO$_2$ and XeF$_2$ was then precipitated from the supernatant at −78 °C (see Experimental Section). Prolonged and repeated extractions resulted in dissolution of significant amounts of [NO$_2$][AsF$_6$] and its coextraction with XeF$_2$ and FXeONO$_2$ (see Experimental Section).

The ^{19}F NMR spectrum of a SO$_2$ClF solution containing extracted FXeONO$_2$ and XeF$_2$ was monitored at 0 °C and showed that FXeONO$_2$ was 50% decomposed after 6.5 h when the decomposition was quenched at −40 °C. The only fluorine-containing decomposition product observed was XeF$_2$ (−177.6 ppm, $^1J_{^{19}\mathrm{F}-^{129}\mathrm{Xe}}$ = 5611 Hz). Low-temperature Raman spectra of FXeONO$_2$ in admixture with XeF$_2$ and [NO$_2$][AsF$_6$] (Figure S2, Supporting Information) revealed that FXeONO$_2$ had partially decomposed to N$_2$O$_5$ and presumably XeF$_2$ at −50 °C after 5 h, whereas FXeONO$_2$ had partially decomposed to N$_2$O$_4$ and XeF$_2$·N$_2$O$_4$ at −78 °C after 7 days. The former decomposition pathway, leading to N$_2$O$_5$, likely proceeds through the unstable intermediate, O$_2$NOONO$_2$ (eq 2), which is known to rapidly decompose at −78 °C according to eq 3,[24,25] and by analogy with the decomposition of FXeOSO$_2$F to XeF$_2$, FO$_2$SOOSO$_2$F, and Xe.[5]

$$2\mathrm{FXeONO_2} \rightarrow \mathrm{XeF_2} + [\mathrm{O_2NOONO_2}] + \mathrm{Xe} \tag{2}$$

$$[\mathrm{O_2NOONO_2}] \rightarrow \mathrm{N_2O_5} + {}^1\!/_2\mathrm{O_2} \tag{3}$$

The latter decomposition pathway, leading to N$_2$O$_4$ and XeF$_2$·N$_2$O$_4$, may occur through the unstable *N*-nitrito or *O*-nitrito intermediates, FXeNO$_2$ (eq 4) and FXeONO (eq 5), which would most likely decompose according to eqs 6−8 and eqs 9 and 10, respectively.

$$\mathrm{FXeONO_2} \rightarrow [\mathrm{FXeNO_2}] + {}^1\!/_2\mathrm{O_2} \tag{4}$$

$$\mathrm{FXeONO_2} \rightarrow [\mathrm{FXeONO}] + {}^1\!/_2\mathrm{O_2} \tag{5}$$

$$2[\mathrm{FXeNO_2}] \rightarrow \mathrm{XeF_2} + \mathrm{Xe} + \mathrm{N_2O_4} \tag{6}$$

$$\mathrm{XeF_2} + \mathrm{N_2O_4} \rightarrow \mathrm{XeF_2\cdot N_2O_4} \tag{7}$$

$$[\mathrm{FXeNO_2}] \rightarrow \mathrm{Xe} + \mathrm{NO_2F} \tag{8}$$

$$2[\mathrm{FXeONO}] \rightarrow \mathrm{XeF_2} + \mathrm{Xe} + \mathrm{N_2O_4} \tag{9}$$

$$[\mathrm{FXeONO}] \rightarrow \mathrm{Xe} + \mathrm{NO_2F} \tag{10}$$

The gas-phase thermochemical calculations using the MP2 method (Table S2, Supporting Information) support the proposed decomposition pathways. The decomposition pathway for FXeONO$_2$ that leads to XeF$_2$, N$_2$O$_5$ (via N$_2$O$_6$), and Xe (eqs 2 and 3) was found to be spontaneous under standard conditions ($\Delta G°$ = −75.7 kJ mol^{-1}) and at −78 °C ($\Delta G_{195.15}$ = −71.0 kJ mol^{-1}) for the decomposition of 1 mol of FXeONO$_2$ to XeF$_2$, N$_2$O$_6$, and Xe. A further −22.5 kJ mol^{-1} ($\Delta G_{195.15}$ = −17.9 kJ mol^{-1}) is released when 0.5 mol of N$_2$O$_6$ decomposes to N$_2$O$_5$ and O$_2$, giving a net $\Delta G°$ = −98.2 kJ mol^{-1} ($\Delta G_{195.15}$ = −88.9 kJ mol^{-1}) for the decomposition of 1 mol of FXeONO$_2$. The remaining proposed pathways, which involve the nonspontaneous generation of FXeNO$_2$ (eq 4, $\Delta G°$ = 26.5 kJ mol^{-1}, $\Delta G_{195.15}$ = 35.7 kJ mol^{-1}) or FXeONO (eq 5, $\Delta G°$ = 37.9 kJ mol^{-1}, $\Delta G_{195.15}$ = 46.5 kJ mol^{-1}) as intermediates, are more than compensated for by their spontaneous decompositions to XeF$_2$, Xe, and N$_2$O$_4$ (FXeNO$_2$ [one-half of eq 6], $\Delta G°$ = −139.2 kJ mol^{-1}, $\Delta G_{195.15}$ = −136.3 kJ mol^{-1}; FXeONO [one-half of eq 9], $\Delta G°$ = −150.6 kJ mol^{-1}, $\Delta G_{195.15}$ = −147.1 kJ mol^{-1}) or to NO$_2$F and Xe (FXeNO$_2$ [eq 8], $\Delta G°$ = −217.6 kJ mol^{-1}, $\Delta G_{195.15}$ = −207.4 kJ mol^{-1}; FXeONO [eq 10], $\Delta G°$ = −229.0 kJ mol^{-1}, $\Delta G_{195.15}$ = −218.2 kJ mol^{-1}).

2.2. Reactions of XeF$_2$ with HNO$_3$. Attempts were made to prepare FXeONO$_2$ and Xe(ONO$_2$)$_2$ by reaction of XeF$_2$ with HNO$_3$. Xenon difluoride was allowed to react with 2 equiv of 100% HNO$_3$ in SO$_2$ClF solution. NMR spectroscopy at −30 °C in SO$_2$ClF solution revealed XeF$_2$ (−1684 ppm, $^1J_{^{19}\mathrm{F}-^{129}\mathrm{Xe}}$ = 5630 Hz) and Xe gas (−5374 ppm) in the ^{129}Xe spectrum and only XeF$_2$ (−183.4 ppm, $^1J_{^{19}\mathrm{F}-^{129}\mathrm{Xe}}$ = 5633 Hz) and HF (−180.2 ppm, $\Delta\nu_{1/2}$ = 550 Hz) in the ^{19}F spectrum. Although the gas-phase syntheses (Table S2, Supporting Information) of FXeONO$_2$ (eq 11, $\Delta G°$ = −17.6 kJ mol^{-1}, $\Delta G_{195.15}$ = −20.2 kJ mol^{-1}) and Xe(ONO$_2$)$_2$ (eq 12, $\Delta G°$ = −17.5 kJ mol^{-1}, $\Delta G_{195.15}$ = −20.8 kJ mol^{-1}) are near equilibrium, their rapid decompositions (FXeONO$_2$, eqs 2 and 3 or eqs 4−10; Xe(ONO$_2$)$_2$, eq 13 followed by eq 3) may preclude their observation by NMR spectroscopy.

$$\mathrm{XeF_2} + \mathrm{HNO_3} \rightarrow \mathrm{FXeONO_2} + \mathrm{HF} \tag{11}$$

$$\mathrm{FXeONO_2} + \mathrm{HNO_3} \rightarrow \mathrm{Xe(ONO_2)_2} + \mathrm{HF} \tag{12}$$

$$\mathrm{Xe(ONO_2)_2} \rightarrow \mathrm{O_2NOONO_2} + \mathrm{Xe} \tag{13}$$

Although FXeONO$_2$ and/or Xe(ONO$_2$)$_2$ could account for the decomposition products observed by NMR spectroscopy, in either case, the degree of reaction must have been small because neither decomposition product, N$_2$O$_4$ or N$_2$O$_5$, was observed in the Raman spectrum. Rather, XeF$_2$·HNO$_3$ crystallized between −40 and −60 °C from SO$_2$ClF solution and was characterized in the solid state by Raman spectroscopy and by single-crystal X-ray diffraction (see X-ray Crystallography and Raman Spectroscopy). These findings indicate that if Xe(ONO$_2$)$_2$ forms, it is inherently unstable toward decomposition. The gas-phase thermochemical calculations (Table S2, Supporting Information) show a large negative Gibbs free energy for the spontaneous decomposition of Xe(ONO$_2$)$_2$ to Xe and the unstable intermediate, N$_2$O$_6$ (eq 13, $\Delta G°$ = −151.4 kJ mol^{-1}, $\Delta G_{195.15}$ = −141.4 kJ mol^{-1}).

2.3. Reactions of XeF$_2$ and [XeF][AsF$_6$] with N$_2$O$_5$. Attempts to react XeF$_2$ or [XeF][AsF$_6$] with N$_2$O$_5$ in SO$_2$ClF to give FXeONO$_2$ and/or Xe(ONO$_2$)$_2$ were monitored by Raman spectroscopy. A 1.5:1 mixture of XeF$_2$ and N$_2$O$_5$ that was warmed stepwise from −40 to 10 °C showed essentially no reaction, with only a small amount of N$_2$O$_5$ decomposition to N$_2$O$_4$ and subsequent formation of XeF$_2$·N$_2$O$_4$ (vide infra). However, at −78 °C, equimolar amounts of [XeF][AsF$_6$] and N$_2$O$_5$ formed a transient orange, clumpy mixture which was consistent with [Xe$_3$OF$_3$][AsF$_6$] formation (eq 14). Gradual warming of the reaction mixture above −30 °C to completely

---

(24) Khadzhi-Ogly, M. R.; Yagodovskaya, T. V.; Nekrasov, L. I. *Zh. Fiz. Khim.* **1981**, *55*, 3124–3127.

(25) Khadzhi-Ogly, M. R.; Yagodovskaya, T. V.; Nekrasov, L. I. *Zh. Fiz. Khim.* **1982**, *56*, 1807–1809.

Table 1. NMR Parameters of $FXeONO_2$ and Related Species[a]

solute	solvent	temp, °C	species	$\delta(^{19}F)$, ppm	$\delta(^{129}Xe)$, ppm	$\delta(^{14}N)$, ppm	$^1J_{^{19}F-^{129}Xe}$, Hz
$FXeONO_2$	SO_2ClF	−70	$FXeONO_2$	−131.9	−1974		5456
			XeF_2	−177.3	−1864		5603
$FXeONO_2$	SO_2ClF	−50	$FXeONO_2$			−65.8[b]	
$FXeONO_2$	CH_3CN	−40	$FXeONO_2$	−135.1	−1870		5503
			XeF_2	−179.2	−1775		5697
XeF_2	N_2O_4[c]	30	$FXeONO_2$	−130.1	−1989		5408
			XeF_2	−179.4	−1841		5642
			NO_2F	397.8			
			Xe		−5243		

[a] Unless otherwise noted, the reaction products result from Scheme 1. [b] Attempts to acquire a ^{15}N NMR spectrum on ^{15}N-enriched (98+%) $FXeONO_2$ (SO_2ClF solvent, −70 °C) failed using relaxation delays as long as 180 s. [c] The observed species arise from eqs 16−18.

dissolve N_2O_5 resulted in a white product. Low-temperature Raman spectroscopy showed a mixture of XeF_2, $[NO_2][AsF_6]$, and unreacted N_2O_5 and the absence of $FXeONO_2$. The $[Xe_3OF_3][AsF_6]$ salt, which is unstable above −30 °C,[20] likely decomposed (eq 15) to form XeF_2, O_2, Xe, and $[XeF][AsF_6]$. The latter salt is presumed to re-enter the cycle (eqs 14 and 15) until completely consumed.

$$3[XeF][AsF_6] + N_2O_5 \rightarrow [FXeOXeFXeF][AsF_6] + 2[NO_2][AsF_6] \quad (14)$$

$$[FXeOXeFXeF][AsF_6] \rightarrow XeF_2 + {}^1/_2O_2 + Xe + [XeF][AsF_6] \quad (15)$$

2.4. Reaction of XeF_2 with N_2O_4. Dissolution of XeF_2 in liquid N_2O_4 at 0−30 °C resulted in NO_2F formation (eq 16, $\delta(^{19}F) = 397.8$ ppm at 30 °C). A small, steady-state concentration of $FXeONO_2$ (Table 1) was also observed which apparently arose as a result of the self-ionization of N_2O_4 (eq 17) and the reaction of XeF_2 with NO_3^- (eq 18).

$$N_2O_4 + XeF_2 \rightarrow 2NO_2F + Xe \quad (16)$$

$$N_2O_4 \leftrightarrows NO^+ + NO_3^- \quad (17)$$

$$XeF_2 + NO^+ + NO_3^- \rightarrow FXeONO_2 + NOF \quad (18)$$

The self-ionization of N_2O_4 has been inferred from electrical conductivity measurements ($2.36 \times 10^{-13}\ \Omega^{-1}\ cm^{-1}$ at 17 °C)[26] and by measurement of the self-ionization constant of N_2O_4 in sulfolane at 30 °C ($K_{N_2O_4} = 7.1 \times 10^{-8}$ mol L^{-1}).[27] The small steady-state concentration of the NO_3^- anion (eq 17) and the instability of $FXeONO_2$ (eqs 2−10) at room temperature (vide supra) account for the low product concentrations (see NMR Spectroscopy).

Dissolution of XeF_2 in liquid N_2O_4 at 35 °C also resulted in the formation of $XeF_2 \cdot N_2O_4$, which was observed by Raman spectroscopy of the frozen mixture at −160 °C (see Raman Spectroscopy). The molecular addition compound, $XeF_2 \cdot N_2O_4$, crystallized from a solution of XeF_2 in N_2O_4 at −3 °C and was characterized by single-crystal X-ray diffraction (see X-ray Crystallography).

2.5. Reaction of $FXeONO_2$ with AsF_5. In an attempt to form a salt of the $XeONO_2^+$ cation, a mixture of $FXeONO_2$ and XeF_2 was allowed to react with excess liquid AsF_5 at −78 °C. The reaction was monitored by low-temperature Raman spectroscopy over a period of 24 h and showed that AsF_5 reacted with XeF_2 to yield $[XeF][AsF_6]$, but $FXeONO_2$ did not react. Warming the reaction mixture to −50 °C for 12 h with periodic quenching and monitoring of the spectrum by Raman spectroscopy at −160 °C showed $[XeF][AsF_6]$ and $[NO_2][AsF_6]$ were the only products. The findings are consistent with the formation of an unstable $XeONO_2^+$ salt (eq 19) that rapidly decomposed according to eq 20.

$$FXeONO_{2(s)} + AsF_{5(l)} \rightarrow [XeONO_2][AsF_6]_{(s)} \quad (19)$$

$$[XeONO_2][AsF_6]_{(s)} \rightarrow [NO_2][AsF_6]_{(s)} + Xe_{(g)} + {}^1/_2O_{2(g)} \quad (20)$$

Thermochemical calculations for the gas-phase reactions (Table S2, Supporting Information) show there is a considerable barrier to fluoride ion abstraction from $FXeONO_2$ by AsF_5 to form the $XeONO_2^+$ and AsF_6^- (eq 19 in the gas phase, $\Delta H° = 359.0$ kJ mol^{-1}, $\Delta G° = 365.0$ kJ mol^{-1}; $\Delta H_{195.15} = 358.7$ kJ mol^{-1}, $\Delta G_{195.15} = 362.9$ kJ mol^{-1}), but this barrier is considerably less than that for the gas-phase abstraction of fluoride ion from XeF_2 by AsF_5 ($\Delta H° = 493.2$ kJ mol^{-1}, $\Delta G° = 499.9$ kJ mol^{-1}; $\Delta H_{195.15} = 493.4$ kJ mol^{-1}, $\Delta G_{195.15} = 497.7$ kJ mol^{-1}). Volume-based thermodynamics (VBT) calculations have been used to arrive at the thermodynamic properties of these systems in the solid state (see Solid-State Thermochemistry in the Supporting Information) and show that fluoride ion abstraction is essentially mitigated by the lattice enthalpy of $[XeONO_2][AsF_6]$. Once formed, the gas-phase $XeONO_2^+$ cation has a large negative Gibbs free energy that accompanies its spontaneous decomposition to Xe, O_2, and NO_2^+ (eq 21, $\Delta H° = -142.7$ kJ mol^{-1}, $\Delta G° = -189.5$ kJ mol^{-1}; $\Delta H_{195.15} = -143.0$, $\Delta G_{195.15} = -173.4$ kJ mol^{-1}).

$$XeONO_2{}^+{}_{(g)} \rightarrow Xe_{(g)} + {}^1/_2O_{2(g)} + NO_2{}^+{}_{(g)} \quad (21)$$

The thermochemical parameters were also determined for eq 20 by application of VBT (see Solid State Thermochemistry in the Supporting Information). The appropriate thermochemical cycle (eq 22) using the gas-phase standard enthalpy, $\Delta H°(21)$ (Table S2 in the Supporting Information), and Gibbs free energy, $\Delta G°(21)$, given by eqs 23 and 24 shows that the solid-state decomposition of $[XeONO_2][AsF_6]$ (eq 20) is significantly more exothermic than the gas-phase decomposition of the $XeONO_2^+$ cation (eq 21).

$$\Delta H°(20) = \Delta H°(21) - \Delta H°_L([NO_2][AsF_6]) + \Delta H°_L([XeONO_2][AsF_6]) = -188 \text{ kJ mol}^{-1} \quad (22)$$

$$\Delta S°(20) = S°([NO_2][AsF_6]_{(s)}) + S°(Xe_{(g)}) + {}^1/_2S°(O_{2(g)}) - S°([XeONO_2][AsF_6]_{(s)}) = 207 \text{ J mol}^{-1}\text{ K}^{-1} \quad (23)$$

$$\Delta G°(20) = \Delta H°(20) - T\Delta S°(20) = -250 \text{ kJ mol}^{-1} \quad (24)$$

The gas-phase reaction (eq 25) has also been considered and is shown to be considerably more endothermic ($\Delta H° = 522.0$ kJ mol^{-1}, $\Delta G° = 527.4$ kJ mol^{-1}; $\Delta H_{195.15} = 521.8$ kJ mol^{-1}, $\Delta G_{195.15} = 525.5$ kJ mol^{-1}) than the gas-phase counterpart of

---

(26) Bradley, R. S. *Trans. Faraday Soc.* **1956**, *52*, 1255–1259.
(27) Wartel, M.; Boughriet, A.; Fischer, J. C. *Anal. Chem. Acta* **1979**, *110*, 211–217.

eq 19, and therefore it has not been considered as a likely alternative reaction pathway.

$$FXeONO_2 + AsF_5 \rightarrow XeF^+ + AsF_5ONO_2^- \qquad (25)$$

2.6. Solution Characterization of $FXeONO_2$ by $^{14/15}N$, ^{19}F, and ^{129}Xe NMR Spectroscopy. The ^{19}F and ^{129}Xe NMR spectra of $FXeONO_2$ and XeF_2 mixtures were recorded in SO_2ClF at −70 °C and in CH_3CN at −40 °C, whereas the ^{14}N NMR spectra were recorded in SO_2ClF at −50 °C. The ^{19}F and ^{129}Xe NMR spectra of XeF_2, $FXeONO_2$, and NO_2F were obtained in N_2O_4 solution at 30 °C (see Reaction of XeF_2 with N_2O_4). The NMR parameters for the three solvent systems are provided in Table 1.

The ^{19}F NMR spectrum of $FXeO^{15}NO_2$ (98+% ^{15}N enrichment) in SO_2ClF consisted of a singlet ($\delta(^{19}F) = -131.9$ ppm) with accompanying ^{129}Xe ($I = {}^1/_2$, 26.44%) satellites ($^1J_{^{19}F-^{129}Xe} = 5431$ Hz). No three-bond coupling to ^{15}N ($I = {}^1/_2$) was observed, presumably because the magnitude of $^3J_{^{15}N-^{19}F}$ is relatively small and is obscured by the breadth of the ^{19}F resonance ($\Delta\nu_{1/2} = 13$ Hz at 11.7440 T, $\Delta\nu_{1/2} = 6$ Hz at 7.0463 T).

The ^{129}Xe NMR spectrum of $FXeO^{15}NO_2$ (11.744 T) in SO_2ClF solvent consisted of a doublet arising from $^1J_{^{19}F-^{129}Xe} = 5429$ Hz, which occurred at −1966 ppm in the xenon(II) region of the spectrum. The $^2J_{^{15}N-^{129}Xe}$ coupling presumably was not observed because it was obscured by the line width of the ^{129}Xe resonance ($\Delta\nu_{1/2} = 134$ Hz). In an attempt to reduce contributions to the ^{19}F and ^{129}Xe line widths that result from shielding anisotropy,[28] the ^{129}Xe NMR spectrum was recorded at a lower external field strength (7.0463 T). The line width ($\Delta\nu_{1/2} = 50$ Hz), however, was not narrowed sufficiently to observe the $^2J_{^{15}N-^{129}Xe}$ coupling.

The ^{19}F and ^{129}Xe NMR chemical shifts of $FXeONO_2$ adhere to a nearly linear empirical correlation between ^{19}F and ^{129}Xe NMR chemical shifts of oxygen-bonded FXe−R species (R = OSO_2F, $OS(O)(F)OMoOF_4$, $OS(O)(F)OWOF_4$, $OSeF_5$, $OTeF_5$, $OWOF_5(WOF_4)$, $OWOF_5(WOF_4)_2$)[29] and a correlation between the ^{19}F chemical shifts and $^1J_{^{19}F-^{129}Xe}$ coupling constants that encompasses the majority of xenon fluoride species in the +2, +4, and +6 oxidation states of xenon.[30] No clear-cut correlation exists among the chemical shifts and coupling constants of $FXeOTeF_5$, $FXeONO_2$, XeF_2, and XeF^+ and the corresponding group electronegativities other than their ^{129}Xe chemical shifts (see Supporting Information).

The ^{14}N NMR spectrum in SO_2ClF solvent consisted of a singlet at −65.8 ppm ($\Delta\nu_{1/2} = 50$ Hz). The resonance was quadrupole broadened to an extent that $^3J_{^{14}N-^{19}F}$ and $^2J_{^{14}N-^{129}Xe}$ could not be observed. A ^{15}N NMR study on a ^{15}N-enriched sample of $FXeONO_2$ in the same spectral region was attempted using relaxation delay times as long as 180 s, which did not permit observation of a ^{15}N resonance. The long relaxation time likely results because the ^{15}N atom is bonded to spinless oxygen nuclei which do not provide a dipolar intramolecular spin−lattice relaxation pathway.

The formation of $FXeONO_2$ was also observed at low concentrations by reaction of XeF_2 with N_2O_4 solvent (see Reaction of XeF_2 with N_2O_4). The ^{19}F NMR parameters were found to be similar to those determined in SO_2ClF and CH_3CN solutions (Table 1). Xenon difluoride and NO_2F were also identified in the ^{19}F NMR spectrum, consistent with eq 16, showing that the reaction of XeF_2 with N_2O_4 is slow at 30 °C.

Table 2. Crystallographic Data for $FXeONO_2$, $XeF_2 \cdot HNO_3$, and $XeF_2 \cdot N_2O_4$

chem formula	NO_3FXe	$N_2O_4F_2Xe$	HNO_3F_2Xe
space group	$P2_1/c$	$P\bar{1}$	$Pnma$
a (Å)	4.6663(4)	4.5822(3)	17.3543(7)
b (Å)	8.7995(7)	5.0597(3)	5.6539(2)
c (Å)	9.4153(8)	6.2761(5)	4.7658(2)
α (deg)	90	79.170(7)	90
β (deg)	90.325(5)	88.454(5)	90
γ (deg)	90	81.083(5)	90
V (Å^3)	386.60(6)	141.19(2)	467.62(5)
Z (molecules/unit cell)	4	1	4
mol wt (g mol^{-1})	212.30	261.30	232.30
ρ_{calcd} (g cm^{-3})	3.648	3.073	3.300
T (°C)	−173	−173	−160
μ (mm^{-1})	8.80	6.10	7.32
R_1[a]	0.0417	0.0385	0.0140
wR_2[b]	0.0807	0.0742	0.0317

[a] $R_1 = \sum||F_o| - |F_c||/\sum|F_o|$ for $I > 2\sigma(I)$. [b] wR_2 is defined as $\{\sum[w(F_o^2 - F_c^2)^2]/\sum w(F_o^2)^2\}^{1/2}$ for $I > 2\sigma(I)$.

2.7. X-ray Crystallography. Details of the data collection parameters and other crystallographic information for $FXeONO_2$, $XeF_2 \cdot HNO_3$, and $XeF_2 \cdot N_2O_4$ are given in Table 2. The experimental and calculated bond lengths and angles are summarized in Table 3 and in Table S3 in the Supporting Information.

2.7.1. $FXeONO_2$. The $FXeONO_2$ molecules (Figure 1a), which possess C_s site symmetry, are well-isolated, discrete molecular units as inferred from the long intermolecular contacts (Table 3 and Figure 1c) and the good agreement between the experimental and calculated geometric parameters and vibrational frequencies (see Computational Results and Raman Spectroscopy). The majority of the Xe···O/F contacts, which range from 3.322(4) to 3.570(5) Å, are near the sum of the van der Waals radii for xenon and fluorine (3.63 Å)[31] and for xenon and oxygen (3.68 Å)[31] and avoid the torus of electron lone pair density about xenon.

The Xe−O bond length (2.126(4) Å) is similar to those found for $FXeOSO_2F$ (2.155(8) Å),[4] $Xe(OTeF_5)_2$ (2.119(11) Å),[32] and $Xe(OSeF_5)_2$ (2.09(3) Å).[32] Correspondingly, the Xe−F bond length (1.992(4) Å) and O−Xe−F angle (177.6(2)°) are similar to those determined for $FXeOSO_2F$ (1.940(8) Å, 177.4(3)°).[4] The Xe−O−N angle (114.7(3)°) was found to be somewhat larger than those determined for $BrONO_2$ (113.8(4)°)[33] and $ClONO_2$ (112.49(4)°),[34] which is attributed to decreased oxygen lone electron pair−oxygen bond pair repulsions and is in accordance with the bond order trend Xe−O < Br−O < Cl−O (Table S4, Supporting Information). The geometric parameters of the ONO_2 groups in $FXeONO_2$ and $XONO_2$ (X = Cl, Br) differ in that the $N-O_S$ bond is shorter than the $N-O_A$ bond in the halogen nitrates, but the opposite trend is observed for $FXeONO_2$ (A denotes anti and S denotes syn about the N−O bridge bond and with respect to the O−Xe−F or O−X groups). The same, but less distinct, bond length trend is found for the

---

(28) Howarth, O. In *Multinuclear NMR*; Mason, J., Ed.; Plenum Press: London, 1987; p 149.

(29) Schrobilgen, G. J.; Holloway, J. H.; Granger, P.; Brevard, C. *Inorg. Chem.* **1978**, *17*, 980–987.

(30) Gerken, M.; Schrobilgen, G. J. *Coord. Chem. Rev.* **2000**, *197*, 335–395.

(31) Bondi, A. *J. Phys. Chem.* **1964**, *68*, 441–451.

(32) Fir, B. A.; Mercier, H. P. A.; Sanders, J. C. P.; Dixon, D. A.; Schrobilgen, G. J. *J. Fluorine Chem.* **2001**, *110*, 89–107.

(33) Minkwitz, R.; Hertel, T. *Z. Naturforsch.* **1997**, *52b*, 1307–1310.

(34) Obermeyer, A.; Borrmann, H.; Simon, A. *J. Am. Chem. Soc.* **1995**, *117*, 7887–7890.

Table 3. Experimental and Calculated[a] Geometric Parameters for $FXeONO_2$, $XeF_2 \cdot HNO_3$, and $XeF_2 \cdot N_2O_4$

$FXeONO_2$	exptl	calcd		exptl	calcd
Bond Lengths (Å)					
Xe(1)−F(1)	1.992(4)	2.018	N(1)−O(2)	1.199(6)	1.200
Xe(1)−O(1)	2.126(4)	2.148	N(1)−O(3)	1.224(6)	1.211
O(1)−N(1)	1.365(7)	1.393			
Bond Angles (°)					
F(1)−Xe(1)−O(1)	177.6(2)	175.5	O(1)−N(1)−O(3)	118.4(5)	117.8
Xe(1)−O(1)−N(1)	114.7(3)	116.0	O(2)−N(1)−O(3)	127.1(5)	129.2
O(1)−N(1)−O(2)	114.5(4)	113.0			
Contacts (Å)					
Xe(1)···F(1A)	3.420(4)		Xe(1)···F(1B)	3.299(4)	
Xe(1)···O(1A)	3.322(4)		Xe(1)···O(2B)	3.545(4)	
Xe(1)···O(2A)	3.478(4)		Xe(1)···O(3B)	3.570(5)	
Xe(1)···O(3A)	3.390(4)		Xe(1)···O(3C)	3.518(4)	
N(1)···F(1A)	2.780(6)		O(1)···F(1A)	2.935(5)	
O(2)···N(1A)	2.923(6)		Xe(1)···O(3)	2.965(7)	3.024

$XeF_2 \cdot HNO_3$	exptl	calcd		exptl	calcd
Bond Lengths (Å)					
Xe(1)−F(1)	1.9737(8)	1.983	N(1)−O(2)	1.368(2)	1.360
Xe(1)−F(2)	2.0506(8)	2.064	N(1)−O(3)	1.216(2)	1.220
O(1)−N(1)	1.206(2)	1.193	O(2)−H(1)	0.83(2)	1.016
Bond Angles (°)					
F(1)−Xe(1)−F(2)	178.98(3)	176.9	O(2)−N(1)−O(3)	117.2(1)	116.3
O(1)−N(1)−O(2)	114.6(1)	115.6	N(1)−O(2)−H(1)	106(2)	104.1
O(1)−N(1)−O(3)	128.2(1)	128.1			
Contacts (Å)					
H(1)···F(2)	1.86(2)	1.520	Xe(1)···F(1B)	3.3050(4)	
Xe(1)···O(3)	3.317(1)	3.034	Xe(1)···F(1C)	3.3050(4)	
Xe(1)···F(1A)	3.4897(9)		Xe(1)···O(1B)	3.4156(6)	
Xe(1)···O(1A)	3.4156(6)		Xe(1)···O(1C)	3.456(1)	
Xe(1)···F(2A)	3.4859(8)		Xe(1)···O(2B)	3.5284(6)	
Xe(1)···O(2A)	3.5284(6)		O(2)···F(2)	2.690(1)	2.536

$XeF_2 \cdot N_2O_4$			calcd[b]	
	exptl		model A	model B
Bond Lengths (Å)				
Xe(1)−F(1)	1.985(3)	Xe(1)−F(1)	2.025	2.015
		Xe(1)−F(2)	2.003	2.010
N(1)−O(1)	1.194(6)	N(1)−O(1)	1.187	1.186
N(1)−O(2)	1.182(6)	N(1)−O(2)	1.184	1.186
		N(2)−O(3)	1.187	1.185
		N(2)−O(4)	1.184	1.185
N(1)−N(1A)	1.738(8)	N(1)−N(2)	1.792	1.799
Bond Angles (°)				
F(1)−Xe(1)−F(1A)	180.0	F(1)−Xe(1)−F(2)	179.7	179.8
O(1)−N(1)−N(1A)	112.5(4)	O(1)−N(1)−N(2)	112.7	112.8
		O(2)−N(1)−N(2)	112.7	112.8
O(2)−N(1)−N(1A)	113.0(4)	O(3)−N(2)−N(1)	112.7	112.5
		O(4)−N(2)−N(1)	112.7	112.5
O(1)−N(1)−O(2)	134.5(5)	O(1)−N(1)−O(2)	134.6	134.4
		O(3)−N(2)−O(4)	134.6	134.9
Contacts (Å)				
F(1)···N(1B)	2.720(4)	F(1)···N(1)	2.910	3.245
F(1)···N(1C)	2.834(5)	F(1)···N(2)	2.910	
Xe(1)···F(1B)	3.370(3)			
Xe(1)···F(1C)	3.370(3)			
Xe(1)···O(1B)	3.516(4)			
Xe(1)···O(1D)	3.440(4)			
Xe(1)···O(2)	3.490(4)			
Xe(1)···O(2C)	3.490(4)	Xe(1)···O(1)	4.003	3.854
Xe(1)···O(2E)	4.180(4)	Xe(1)···O(2)		3.854
Xe(1)···O(1C)	3.440(4)	Xe(1)···O(3)	4.003	
Xe(1)···O(1E)	3.516(4)			
Xe(1)···O(2B)	3.435(4)			
Xe(1)···O(2D)	3.435(4)			
Xe(1)···O(2F)	4.180(4)			

[a] B3LYP/aug-cc-pVTZ(-PP). [b] Calculated geometric parameters for N_2O_4 coordinated to XeF_2 through two oxygen atoms bound to two different nitrogen atoms (model A) and two oxygen atoms bound to the same nitrogen atom (model B).

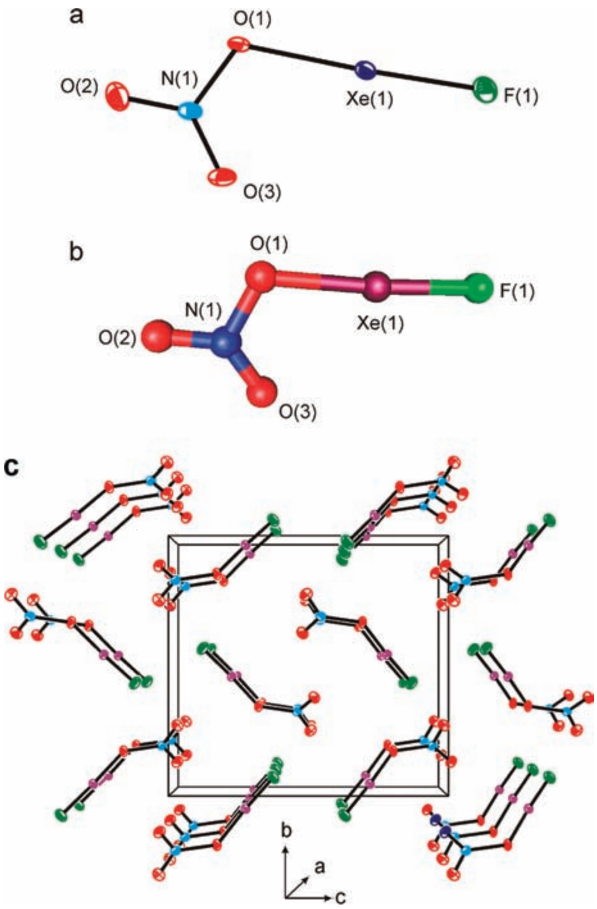

Figure 1. (a) X-ray crystal structure of $FXeONO_2$. Thermal ellipsoids are shown at the 50% probability level. (b) Calculated geometry of $FXeONO_2$. The atom numbering scheme corresponds to that used in Table 3. (c) Packing diagram for $FXeONO_2$ viewed along the *a*-axis.

calculated $N-O_S$ and $N-O_A$ bond lengths. These experimental bond length trends agree with the relative, but opposite, bond order trends calculated at the B3LYP/aug-cc-pVTZ(-PP) and MP2/aug-cc-pVTZ(-PP) levels of theory. However, the bond orders are nearly equal for $FXeONO_2$ at the MP2 level of theory (Table S4).

2.7.2. $XeF_2 \cdot HNO_3$. The structure of $XeF_2 \cdot HNO_3$ (Figure 2) is only the second example of a hydrogen-bonded XeF_2 adduct, the other being $[H_3O \cdot 2XeF_2][AsF_6]$.[20] All atoms are coplanar, allowing the molecules to form sheets in the *a*,*c*-plane comprised of alternating XeF_2 and HNO_3 molecules that are congruently stacked along the *b*-axis (Figure 3 and Figure S3 in the Supporting Information). The packing arrangement in the *a*,*c*-plane is largely determined by the short H···F (1.86(2) Å) contacts and weak Xe···O(3) (3.317(1) Å) contacts, which are significantly less than the sums of the van der Waals radii (2.67 and 3.68 Å, respectively).[31] The strong hydrogen bond distorts the local symmetry of the XeF_2 molecule from $D_{\infty h}$ to $C_{\infty v}$ symmetry. The Xe−F bond length distortions (terminal (F_t), 1.9737(8) Å; bridge (F_b), 2.0506(8) Å) parallel the distortions found in compounds where XeF_2 is homoleptically coordinated to a metal ion through a single fluorine bridge. The present $Xe-F_b$ and $Xe-F_t$ bond lengths are comparable to those in $[Ca(XeF_2)_5][PF_6]_2$,[35] $[Cd(XeF_2)_5][PF_6]_2$,[35] $[Cd(XeF_2)][BF_4]_2$,[36] $[Mg(XeF_2)_4][AsF_6]_2$,[37] $[Mg(XeF_2)_2][AsF_6]_2$,[37] and $[Ca_2(XeF_2)_9][AsF_6]_4$,[38] where the $Xe-F_b$ bonds range from 2.026(7) to 2.087(8) Å and the $Xe-F_t$ bonds range from 1.913(5) to 1.966(6) Å. The geometric parameters obtained for HNO_3 in the present structure ($N-O_H$,

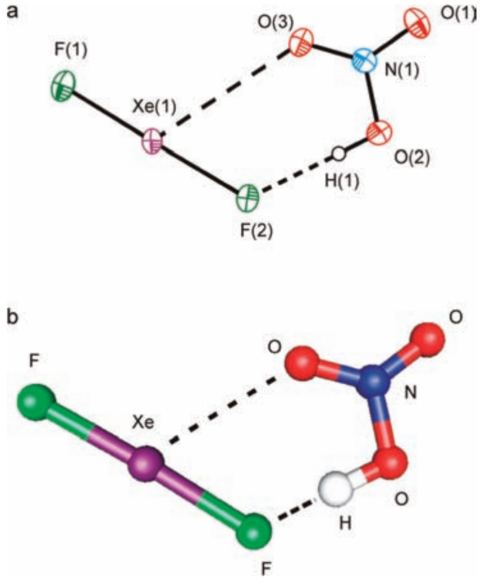

Figure 2. (a) X-ray crystal structure of $XeF_2 \cdot HNO_3$ showing the $H\cdots F$ and $Xe\cdots O$ contacts. Thermal ellipsoids are shown at the 70% probability level. (b) Calculated geometry of $XeF_2 \cdot HNO_3$. The atom numbering scheme corresponds to that used in Table 3.

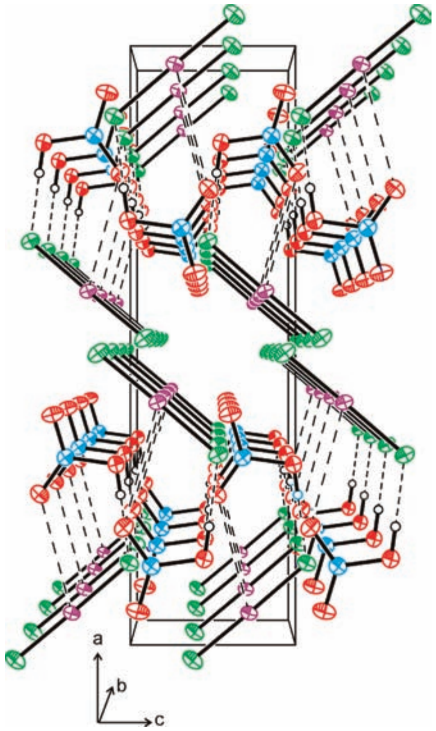

Figure 3. Packing diagram of $XeF_2 \cdot HNO_3$ viewed along the *b*-axis, showing the interactions between the XeF_2 and HNO_3 molecules. Thermal ellipsoids are shown at the 70% probability level.

1.368(2) Å; $N-O_S$, 1.216(2) Å; $N-O_A$, 1.206(2) Å; O_S-N-O_A, 128.2(1)°) are of higher precision when compared with the previous structure of anhydrous HNO_3 ($N-O_H$, 1.41(2) Å; $N-O_S = N-O_A$, 1.22(2) Å; O_S-N-O_A, 130(5)°),[39] although they do not differ by more than $\pm 3\sigma$.

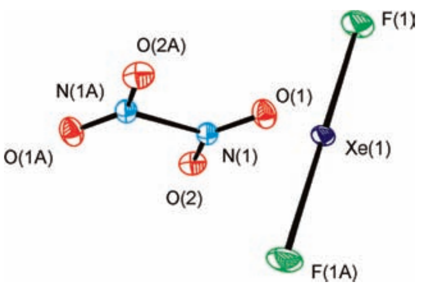

Figure 4. X-ray crystal structure of the $XeF_2 \cdot N_2O_4$ molecular addition compound. Thermal ellipsoids are shown at the 50% probability level. The atom numbering scheme corresponds to that used in Table 3.

2.7.3. $XeF_2 \cdot N_2O_4$. The XeF_2 molecule of $XeF_2 \cdot N_2O_4$ (Figure 4) is constrained by crystal symmetry to $D_{\infty h}$ symmetry and possesses an Xe−F bond length of 1.985(3) Å, which does not differ significantly from the bond length determined for crystalline XeF_2 at −173 °C (1.999(4) Å).[40] Although the N_2O_4 molecules were found to have local C_{2v} symmetry (N−O, 1.194(6) and 1.182(6) Å; N−N, 1.738(8) Å; O−N−O, 134.5(5)°), the N−O bond lengths do not differ by more than $\pm 3\sigma$, and thus they may be regarded as having D_{2h} symmetry. The absence of additional bands in the Raman spectrum resulting from symmetry lowering and destruction of the center of symmetry (see Raman Spectroscopy) indicates retention of high (D_{2h}) symmetry by N_2O_4. There is close agreement between the geometric parameters of N_2O_4 in $XeF_2 \cdot N_2O_4$ and those determined from the crystal structure of N_2O_4 at 100 K (N−O, 1.1855(9) Å; N−N, 1.7560(14) Å; O−N−O, 134.46(12)°).[41]

Six N_2O_4 molecules are coordinated to each XeF_2 molecule through their oxygen ligand atoms. Three coordination modalities occur: a bidentate interaction with two oxygen atoms bound to different nitrogen atoms (3.435(4) and 3.516(4) Å) of the same N_2O_4 molecule, a bidentate interaction with two oxygen atoms bound to the same nitrogen atom (3.440(4) and 4.180(4) Å), and an interaction with a single oxygen atom (3.490(4) Å) (Figure 5a). Although the long contacts differ significantly from the two bidentate interactions calculated for the gas-phase adduct (Figure 5b), the bidentate interaction resulting from each oxygen atom bound to different nitrogen atoms was found to be 6.5 kJ mol^{-1} more stable than the bidentate interaction with both oxygen atoms bound to the same nitrogen atom. There are also two long contacts between xenon and two fluorine atoms of different XeF_2 molecules (3.370(3) Å) that are somewhat less than the sum of the Xe and F van der Waals radii (3.63 Å).[31] Two long $F\cdots N$ contacts were also observed at 2.720(4) and 2.834(5) Å (cf. sum of the F and N van der Waals radii, 3.02 Å).[31]

2.8. Raman Spectroscopy. The low-temperature, solid-state Raman spectra of $FXeONO_2$, $XeF_2 \cdot HNO_3$, and $XeF_2 \cdot N_2O_4$ are depicted in Figures 6 and 7. The experimental and calculated frequencies and their assignments are listed in Tables 4−7 and Tables S5−S7 in the Supporting Information.

---

(35) Bunič, T.; Tavčar, G.; Tramšek, M.; Žemva, B. *Inorg. Chem.* **2006**, *45*, 1038–1042.

(36) Tavčar, G.; Žemva, B. *Inorg. Chem.* **2005**, *44*, 1525–1529.

(37) Tramšek, M.; Benkič, T.; Žemva, B. *Inorg. Chem.* **2004**, *43*, 699–703.

(38) Tramšek, M.; Benkič, T.; Žemva, B. *Angew. Chem., Int. Ed.* **2004**, *43*, 3456–3458.

(39) Luzzati, P. V. *Acta Crystallogr.* **1951**, *4*, 120–131.

(40) Elliott, H. St. A.; Lehmann, J. F.; Mercier, H. P. A.; Jenkins, H. D. B.; Schrobilgen, G. J. *Inorg. Chem.* **2010**; DOI: 10.1021/ic101152x (in press).

(41) Kvick, Å.; McMullan, R. K.; Newton, M. D. *J. Chem. Phys.* **1982**, *76*, 3754–3761.

(42) Guillory, W. A.; Bernstein, M. L. *J. Chem. Phys.* **1975**, *62*, 1058–1060.

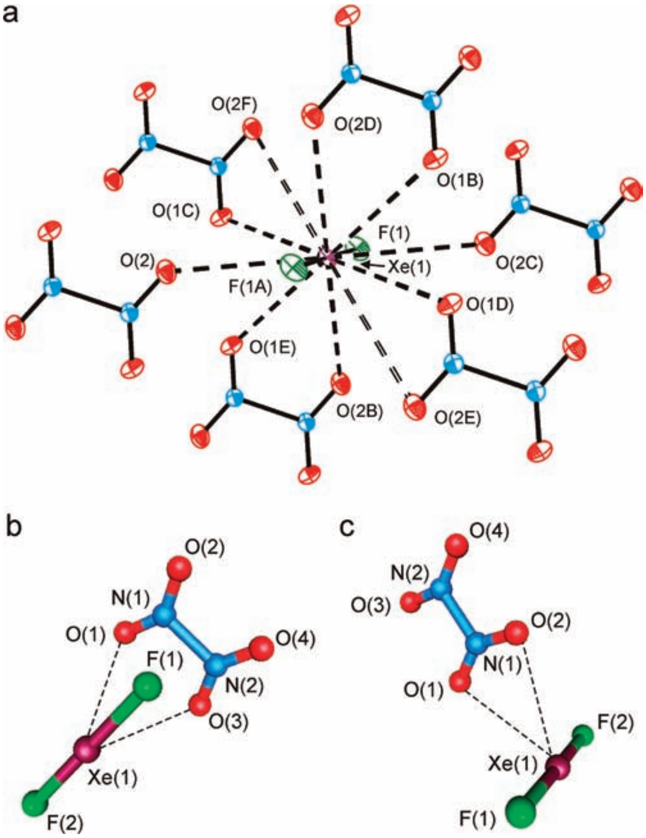

Figure 5. (a) Local environment of the XeF_2 molecule in the crystal structure of $XeF_2 \cdot N_2O_4$, showing the three unique coordination pathways to the xenon atom from N_2O_4. (b,c) Calculated geometries of N_2O_4 coordinated to the xenon atom of XeF_2 through two oxygens bound to (b) two different nitrogen atoms (model A) and (c) the same nitrogen atom (model B). The numbering scheme corresponds to that used in Table 3.

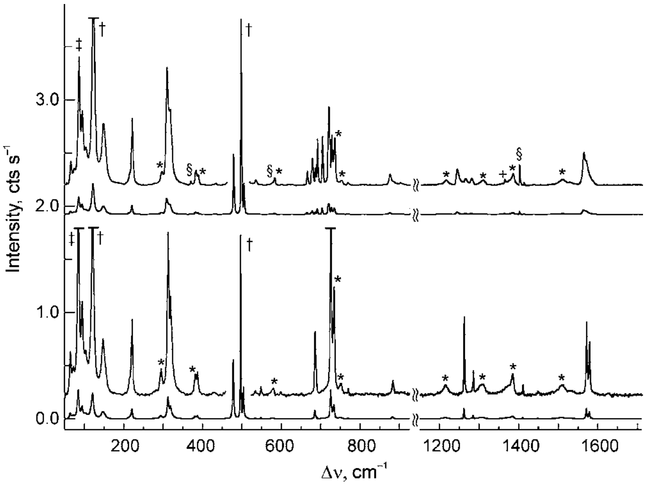

Figure 6. Raman spectra of natural abundance FXe^{16}ON^{16}O$_2$ (lower trace) and 98.6% ^{18}O-enriched FXe^{16}ON(^{16}O^{18}O) (upper trace) recorded at −160 °C using 1064-nm excitation. Symbols denote XeF_2 (†), FEP (*), laser artifact (‡), [NO_2][AsF_6] (§), and [^{18}ON^{16}O][AsF_6] (+).

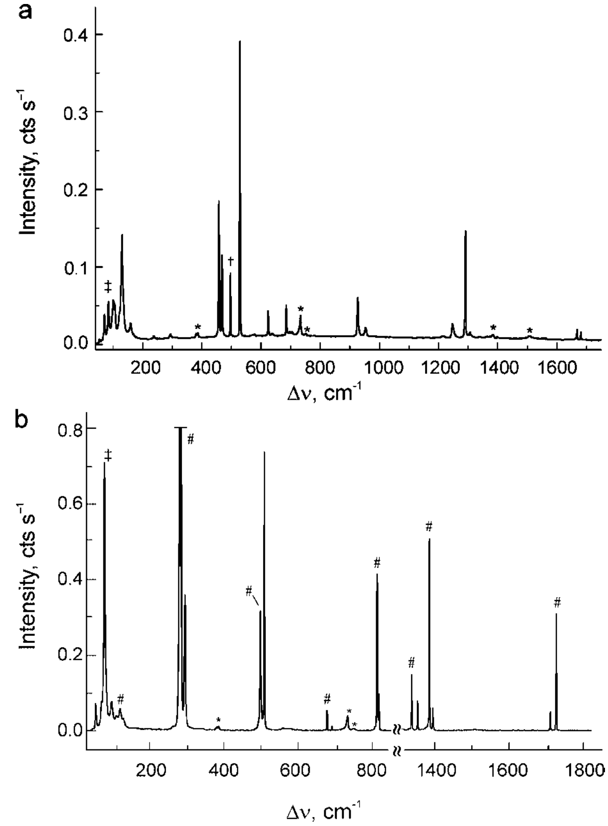

Figure 7. Raman spectra recorded at −160 °C using 1064-nm excitation: (a) solid $XeF_2 \cdot HNO_3$ and (b) solid $XeF_2 \cdot N_2O_4$ recorded under frozen N_2O_4 solution. Symbols denote XeF_2 (†), FEP (*), laser artifact (‡), and N_2O_4 (#).

The spectral assignments for FXe^{16}O^{14}N^{16}O$_2$, FXe^{16}O^{14}N(^{16}O^{18}O), and FXe^{16}O^{15}N^{16}O$_2$ were made by comparison with the calculated frequencies and Raman intensities for all possible $^{16/18}$O-isotopomers (Table 5). The spectra were calculated using the aug-cc-pVTZ(-PP) basis set at the B3LYP, PBE1PBE, and MP2 levels of theory and reproduced the experimental trends at all levels (see Computational Results, Table 5, and Table S5 in the Supporting Information). Calculated values referred to in the ensuing discussion are those obtained by the B3LYP method. Assignments for $XeF_2 \cdot HNO_3$ and $XeF_2 \cdot N_2O_4$ were made by comparison with the calculated frequencies and Raman intensities (Tables 6 and 7 and Tables S6 and S7 in the Supporting Information) of the energy-minimized geometries (Figures 2b and 5b,c) and by comparison with those of XeF_2 (Table S8, Supporting Information), HNO_3 (Tables S9 and S10, Supporting Information), and N_2O_4 (Tables S11 and S12, Supporting Information).

2.8.1. FXeONO$_2$. The FXeONO$_2$ molecule (C_s symmetry) possesses 12 fundamental vibrational modes that span the irreducible representations 9A′ + 3A″, which are Raman and infrared active. The four FXeONO$_2$ molecules in the crystallographic unit cell have C_1 site symmetry. A factor-group analysis for FXe^{16}ON^{16}O$_2$ (Table S13, Supporting Information) predicts that each gas-phase Raman- and infrared-active mode of FXeONO$_2$ is split, as a result of vibrational mode coupling within the centrosymmetric unit cell (C_{2h} unit cell symmetry), into a maximum of two Raman-active (A$_g$ and B$_g$) and two infrared-active (A$_u$ and B$_u$) components. Accordingly, two components were resolved for every stretching mode of the natural abundance molecule except for $\nu(O_{Xe}-N) + \delta(NO_2)$.

Vibrational frequencies calculated at all levels of theory (Table 5 and Table S5 in the Supporting Information) reproduced the experimental frequency and $^{16/18}$O isotopic shift trends for FXe^{16}O^{14}N^{16}O$_2$, FXe^{16}O^{14}N(^{16}O^{18}O), and FXe^{16}O^{15}N^{16}O$_2$ given in Table 4. The calculations clearly show that the experimental ^{18}O-enriched spectrum is not that of FXe^{18}ON^{16}O$_2$

Table 4. Experimental Raman Frequencies and Intensities for $FXe^{16}O^{14}N^{16}O_2$, $FXe^{16}O^{14}N(^{16}O^{18}O)$, and $FXe^{16}O^{15}N^{16}O_2$

frequencies, cm^{-1}					
$FXe^{16}O^{14}N^{16}O_2$	$FXe^{16}O^{14}N(^{16}O^{18}O)$		$FXe^{16}O^{15}N^{16}O_2$		
exptl[a,b]	exptl[a,c]	$\Delta\nu^{16/18}$ [d]	exptl[a]	$\Delta\nu^{14/15}$ [e]	assgnt (C_s)[f]
1578.8(12)	1567.4br(6)	−11.4	1543.2(1)	−35.6	$\nu_1(A')$, ν(NO − NO)
1571.7(16)	1561.8br(7)	−9.9	1536.6(2)	−35.1	
	1278.7br(2)	−16.6	1246.7(8)	−15.4	$\nu_2(A')$, ν(NO + NO)
1285.5(5)	1263.2br(2)				
1262.1(17)	1244.6sh				
	1242.5br(4)				
882.9(3)	873.4br(2)	−9.5			$\nu_3(A')$, $\nu(O_{Xe}{-}N) + \delta(NO_2)$
769.4(2)	766.1(1)	−3.3			$\nu_{10}(A'')$, $\rho_w(NO_3)$
725.5(49)	725.2(11)	−9.9 (av)	723.2(8)	−2.3	$\nu_4(A')$, $\delta(O_{Xe}{-}N{-}O) + \rho_r(NO_2)$
	718.4(18)				
	717.1(17)				
	701.6(11)				
685.4(15)	684.3(4)	−10.9 (av)	690.3(100)[g]	1.5	$\nu_5(A')$, $\nu(O_{Xe}{-}N) - \delta(NO_2)$
	676.6(6)		683.5(61)		
	674.1(3)				
	663.1(3)				
503.8(54)	503.5(54)	−0.3	503.6(14)	−0.2	$\nu_6(A')$, ν(Xe−F)
478.1(100)	477.0(100)	−1.1	478.4(73)	0.3	
318.9(23)	315.0(17)	−3.9	317.9(4)	−1.0	$\nu_7(A')$, $\nu(Xe{-}O) + \rho_r(NO_3)$
312.7(37)	307.2(26)	−5.5	310.9(14)	−1.8	
220.6(15)	218.6(15)	−2.0	220.3(10)	−0.3	$\nu_{11}(A'')$, ρ_w(F−Xe−O)
146.9(14)	145.4(11)	−1.5	146.4(8)	−0.5	$\nu_8(A')$, $\delta(F{-}Xe{-}O) + \rho_r(NO_3)$
102.2(11)	101.1(8)	−1.1			$\nu_9(A')$, $\delta(F{-}Xe{-}O) - \rho_r(NO_3)$
93.6(16)	91.7(17)	−1.9			
64.3(11)	62.8(5)	−1.5			$\nu_{12}(A'')$, ρ_t about Xe−O bond

[a] The Raman spectra were recorded in FEP sample tubes at −160 °C using 1064-nm excitation. Relative Raman intensities are given in parentheses. The spectra of $FXe^{16}O^{14}N^{16}O_2$ and $FXe^{16}O^{14}N(^{16}O^{18}O)$ were recorded for the solid products extracted from the product mixture using SO_2ClF solvent. The spectrum of $FXe^{16}O^{15}N^{16}O_2$ was recorded for the nonextracted reaction mixture. Abbreviations denote shoulder (sh) and broad (br). [b] Two bands were also observed at 1448.3(<1) and 1410.3(2) cm^{-1} and were tentatively assigned to combination modes. [c] Two bands were also observed at 1436.1(<1) and 1410.7(1) cm^{-1} and were tentatively assigned to combination modes. A third band at 1362.4(1) cm^{-1} was assigned to the in-phase $^{18}ON^{16}O$ stretch of $[^{18}ON^{16}O][AsF_6]$. [d] $\Delta\nu^{16/18} = \nu(^{18}O) - \nu(^{16}O)$. The abbreviation denotes average (av). [e] $\Delta\nu^{14/15} = \nu(^{15}N) - \nu(^{14}N)$. [f] Abbreviations denote stretch (ν), bend (δ), twist (ρ_t), wag (ρ_w), and rock (ρ_r). Bond elongations and angle openings are denoted by plus (+) signs, and bond contractions and angle closings are denoted by minus (−) signs. [g] The band is coincident with the $\nu_1(A_{1g})$ band of AsF_6^-.

because, in this case, near-zero isotopic shifts are predicted for $\nu_1(A')$, ν(NO − NO) and $\nu_2(A')$, ν(NO + NO) at 1576 and 1274 cm^{-1}, respectively. The $FXe^{18}ON(^{16}O_A{}^{18}O_S)$ and $FXe^{18}ON(^{16}O_S{}^{18}O_A)$ conformers (A denotes ^{18}O anti and S denotes ^{18}O syn about the N−O bridge bond and with respect to the O−Xe−F group) are also eliminated because, in contrast with the observed average $^{16/18}O$ isotopic shifts of −9.9 and −10.9 cm^{-1}, respectively, a significantly larger isotopic shift (−31 cm^{-1}) is predicted for both $\nu_4(A')$ and $\nu_5(A')$. The experimental ^{18}O-enriched spectrum has therefore been assigned to an equimolar mixture of $FXe^{16}ON(^{16}O_A{}^{18}O_S)$ and $FXe^{16}ON(^{16}O_S{}^{18}O_A)$ conformers and establishes that scrambling of ^{18}O among the bridge site and terminal sites does not occur.

The Raman spectra of $FXe^{16}ON(^{16}O_A{}^{18}O_S)$ and $FXe^{16}ON(^{16}O_S{}^{18}O_A)$ exhibit levels of complexity that are not reproduced by the calculated spectra. The calculations show that the only modes where the *syn*- and *anti*-conformers might be differentiated are ν_1 and ν_2, with calculated splittings of 7 and 6 cm^{-1}, respectively. However, these splittings are not resolved in the experimental spectra but are manifested on the factor-group split ν_1 and ν_2 bands as significant line broadenings (Figure 6). The attribution of these broadenings to equal populations of the $FXe^{16}ON(^{16}O_A{}^{18}O_S)$ and $FXe^{16}ON(^{16}O_S{}^{18}O_A)$ conformers is supported by the spectrum of $FXe^{16}ON^{16}O_2$ (Figure 6), which displays narrow factor-group split bands for ν_1 and ν_2. Moreover, ^{18}O isotopic enrichment does not result in similar line broadenings on bands other than the symmetric and asymmetric NO_2 stretching bands.

In the case of $FXe^{16}ON(^{16}O^{18}O)$, additional line splittings are observed for ν_1, ν_2, ν_4−ν_7, and ν_9, which are attributed to lowering of the "vibrational unit cell symmetry" of $FXe^{16}ON^{16}O_2$ from C_{2h} symmetry to lower noncentrosymmetric unit cell symmetries. Symmetry lowering in the unit cell results from the combinations and permutations of $FXe^{16}ON(^{16}O_A{}^{18}O_S)$ and $FXe^{16}ON(^{16}O_S{}^{18}O_A)$ isomers that occur among the four vibrationally coupled molecules of the crystallographic unit cell, giving rise to 16 unit cells having the following symmetries (relative weights are given in parentheses): C_{2h} (2), C_i (2), C_s (2), C_2 (2), and C_1 (8). With the exception of the C_{2h} and C_i symmetric cells, the remaining 12 unit cell symmetries are not centrosymmetric with respect to the *syn*-/*anti*-conformations of ^{16}O and ^{18}O in their NO_2 groups. As a consequence, the counterparts of the formally Raman-inactive and infrared-active A_u and B_u components in the factor-group analysis of $FXe^{16}ON^{16}O_2$ are both infrared and Raman active under C_s (A″), C_2 (B), and C_1 (A) unit cell symmetries (Table S13, Supporting Information), potentially doubling the number of factor-group split lines that can be observed when compared with the spectrum of $FXe^{16}ON^{16}O_2$. Although the additional factor-group components that correspond to A_u and B_u under C_{2h} symmetry are not resolved for ν_1, ν_6, ν_7, and ν_9, they are resolved for ν_2, ν_4, and ν_5, which exhibit the predicted four-line splittings

Table 5. Calculated[a] Vibrational Frequencies and Raman and Infrared Intensities for $FXe^{16}ON^{16}O_2$, $FXe^{18}ON^{16}O_2$, $FXe^{16}ON^{18}O_A{}^{16}O_S$, $FXe^{16}ON^{16}O_A{}^{18}O_S$, $FXe^{18}ON^{18}O_A{}^{16}O_S$, $FXe^{18}ON^{16}O_A{}^{18}O_S$, and $FXe^{16}O^{15}N^{16}O_2$[b]

$FXe^{16}ON^{16}O_2$	$FXe^{18}ON^{16}O_2$	$\Delta\nu^{16/18}$ [c]	$FXe^{16}ON^{18}O_A{}^{16}O_S$	$\Delta\nu^{16/18A}$ [d]	$FXe^{16}ON^{16}O_A{}^{18}O_S$	$\Delta\nu^{16/18S}$ [e]	$FXe^{18}ON^{18}O_A{}^{16}O_S$	$\Delta\nu^{16/18-18A}$ [f]	$FXe^{18}ON^{16}O_A{}^{18}O_S$	$\Delta\nu^{16/18-18S}$ [g]	$FXe^{16}O^{15}N^{16}O_2$	$\Delta\nu^{14/15}$ [h]	assgnt
1657.5(63)[329]	1657.3(63)[329]	−0.2	1640.4(58)[314]	−17.1	1647.4(65)[330]	−10.1	1640.1(58)[314]	−17.4	1647.1(65)[330]	−10.4	1619.5(61)[317]	−38.0	$\nu_1(A')$
1300.9(13)[373]	1300.6(14)[379]	−0.3	1279.7(14)[388]	−21.2	1273.8(10)[381]	−27.1	1279.5(14)[394]	−21.4	1273.5(11)[386]	−27.4	1286.1(14)[331]	−14.8	$\nu_2(A')$
880.0(3)[330]	874.1(3)[302]	−5.9	869.3(3)[319]	−10.7	868.3(3)[319]	−11.7	862.6(3)[290]	−17.4	861.7(3)[290]	−18.3	867.1(3)[333]	−12.9	$\nu_3(A')$
782.3(<0.1)[10]	780.3(<0.1)[10]	−2.0	778.3(<0.1)[10]	−4.0	778.3(<0.1)[10]	−4.0	776.3(<0.1)[10]	−6.0	776.3(<0.1)[10]	−6.0	761.9(<1)[10]	−20.4	$\nu_{10}(A'')$
719.3(16)[16]	695.5(12)[13]	−23.8	713.0(15)[15]	−6.3	712.2(18)[22]	−7.1	688.9(11)[11]	−30.4	687.9(14)[18	−31.4	718.0(16)[18]	−1.3	$\nu_4(A')$
666.9(21)[68	642.0(20)[70]	−24.9	659.7(23)[66]	−7.2	659.8(19)[56]	−7.1	635.2(21)[69]	−31.7	635.6(18)[59]	−31.3	666.9(21)[69]	−0.0	$\nu_5(A')$
510.2(54)[255]	510.7(54)[259]	0.5	510.8(55)[254]	0.6	510.9(54)[256]	0.7	510.6(55)[256]	0.4	510.7(54)[258]	0.5	510.9(54)[257]	0.7	$\nu_6(A')$
316.8(28)[31]	311.6(28)[30]	−5.2	310.4(26)[30]	−6.4	315.4(28)[31]	−1.4	305.2(26)[29]	−11.6	309.9(28)[31]	−6.9	316.2(27)[30]	−0.6	$\nu_7(A')$
203.1(<1)[9]	198.7(<1)[9]	−4.4	203.3(<1)[9]	0.2	203.5(<1)[9]	0.4	198.5(<1)[9]	−4.6	198.7(<1)[9]	−4.4	203.5(<1)[9]	0.4	$\nu_{11}(A'')$
198.0(8)[6]	197.7(8)[6]	−0.3	198.3(8)[6]	0.3	195.2(7)[6]	−2.8	197.3(8)[6]	−0.7	194.3(7)[6]	−3.7	198.0(8)[6]	0.0	$\nu_8(A')$
116.1(3)[4]	116.0(3)[4]	−0.1	115.6(3)[4]	−0.5	114.7(3)[4]	−1.4	115.3(3)[4]	−0.8	114.4(3)[4]	−1.7	116.1(3)[4]	0.0	$\nu_9(A')$
73.9(<1)[2]	73.3(<1)[1]	−0.6	72.1(<0.1)[1]	−1.8	73.5(<1)[2]	−0.4	71.4(<1)[1]	−2.5	72.8(<1)[1]	−1.1	74.0(<1)[2]	0.1	$\nu_{12}(A'')$

[a] B3LYP/aug-cc-pVTZ(-PP). Values in parentheses denote Raman intensities (Å^4 u^{-1}). Values in square brackets denote infrared intensities (km mol^{-1}). [b] The notations A and S denote ^{18}O anti and syn, respectively, relative to the O−Xe−F group. [c] $\Delta\nu^{16/18} = \nu(FXe^{18}ON^{16}O_2) - \nu(FXe^{16}ON^{16}O_2)$. [d] $\Delta\nu^{16/18A} = \nu(FXe^{16}ON^{18}O_A{}^{16}O_S) - \nu(FXe^{16}ON^{16}O_2)$. [e] $\Delta\nu^{16/18S} = \nu(FXe^{16}ON^{16}O_A{}^{18}O_S) - \nu(FXe^{16}ON^{16}O_2)$. [f] $\Delta\nu^{16/18-18A} = \nu(FXe^{18}ON^{18}O_A{}^{16}O_S) - \nu(FXe^{16}ON^{16}O_2)$. [g] $\Delta\nu^{16/18-18S} = \nu(FXe^{18}ON^{16}O_A{}^{18}O_S) - \nu(FXe^{16}ON^{16}O_2)$. [h] $\Delta\nu^{14/15} = \nu(FXe^{16}O^{15}N^{16}O_2) - \nu(FXe^{16}ON^{16}O_2)$.

consistent with noncentrosymmetric unit cell symmetries. The vibrational modes of the remaining two centrosymmetric unit cells having C_i symmetry belong to A_g and A_u representations (Table S13). Factor-group analyses of the C_i symmetric cells predict that each vibrational band of free FXeONO$_2$ will be split into two Raman-active A_g and two infrared-active A_u components. As in the case of $FXe^{16}ON^{16}O_2$, the two remaining centrosymmetric unit cells possessing C_{2h} symmetry will give rise to two Raman-active (A_g and B_g) and two infrared-active (A_u and B_u) components (Table S13).

These observations establish that ^{18}O is exclusively terminally bonded to nitrogen and is not scrambled among the terminal and bridge oxygen sites of FXeONO$_2$ when the latter molecule is synthesized by the low-temperature reaction of FXe^{18}OXe---FXeF$^+$ with NO$_2$F, in accordance with the reaction mechanism proposed in Scheme 1. A weak band at 1362 cm^{-1} (Table 4 and Figure 6) also appears in the ^{18}O-enriched spectrum of FXe^{16}ON(^{16}O^{18}O) and the products that result from Scheme 1. The band is assigned to the in-phase ^{18}ON^{16}O stretch of the mixed cation in [^{18}ON^{16}O][AsF$_6$] which arises according to Scheme 2. The band is shifted 34 cm^{-1} to low frequency of ν_s(NO$_2$) in [N^{16}O$_2$][AsF$_6$] and is in good agreement with the calculated ^{18}O isotopic shift of −42 cm^{-1} for ^{18}ON^{16}O$^+$ (Table S14, Supporting Information). Both the out-of-phase ^{18}ON^{16}O stretch and δ(^{18}ON^{16}O) are predicted to be weak, with δ(^{18}ON^{16}O) displaying a small isotopic shift (−6 cm^{-1}), but neither was observed.

The highest frequency modes of natural abundance FXeONO$_2$ occur at 1571.7, 1578.8 cm^{-1} and 1262.1, 1285.5 cm^{-1} and are assigned to the factor-group split ν(NO − NO) and ν(NO + NO) stretches, respectively. These bands exhibit the greatest sensitivity to ^{18}O and ^{15}N substitution, displaying substantial isotopic shifts upon ^{18}O or ^{15}N enrichment (^{18}O, −9.9, −11.4, and −16.6 cm^{-1}, respectively; ^{15}N, −35.1, −35.6, and −15.4 cm^{-1}, respectively), which are in good agreement with the calculated isotopic shifts (^{18}O, −13.6 and −24.2 cm^{-1}; ^{15}N, −38.0 and −14.8 cm^{-1}, respectively). The bands assigned to ν(O$_{Xe}$−N) + δ(NO$_2$) (882.9 cm^{-1}), δ(O$_{Xe}$−N−O) + ρ_r(NO$_2$) (725.5 cm^{-1}), and ν(O$_{Xe}$−N) − δ(NO$_2$) (685.4 cm^{-1}) also exhibit significant sensitivities upon ^{18}O substitution (−9.5, −9.9 and, −10.9 cm^{-1}, respectively), in good agreement with the calculated shifts (−11.2, −6.7 and, −7.1 cm^{-1}, respectively). The band assigned to ρ_w(NO$_3$) (769.4 cm^{-1}) shifts only −3.3 cm^{-1} to lower frequency, in good agreement with the calculated value of −4.4 cm^{-1}. The ν(Xe−F) stretching band is also factor-group split (478.1, 503.8 cm^{-1}) and is readily assigned because it is the most intense feature in the spectrum and because the bands are insensitive to both ^{15}N and ^{18}O substitution.

The bands assigned to ν(Xe−O) + ρ_w(NO$_3$) (312.7, 318.9 cm^{-1}) exhibit a significant ^{16}O/^{18}O isotopic shift (−5.5, −3.9 cm^{-1}), with a much smaller ^{14}N/^{15}N isotopic shift (−1.8, −1.0 cm^{-1}), in agreement with the calculated shifts (^{18}O, −3.9 cm^{-1}; ^{15}N, −0.6 cm^{-1}). The modes occurring below 221 cm^{-1} were readily assigned with the aid of the calculated vibrational frequencies and showed no or very small isotopic dependencies, as expected for low-frequency bending and rocking modes.

2.8.2. XeF$_2$·HNO$_3$. The vibrational spectrum of XeF$_2$·HNO$_3$ was assigned under C_s symmetry. A total of 18 fundamental vibrational modes belonging to the irreducible representations 13A′ + 5A″ are expected, all of which are Raman and infrared active.

The four XeF$_2$·HNO$_3$ molecular units occupy C_s sites in the crystallographic unit cell. The factor-group analysis for the

Table 6. Experimental and Calculated Vibrational Frequencies for $XeF_2 \cdot HNO_3$

frequencies, cm^{-1}				
HNO_3	$XeF_2 \cdot HNO_3$			
exptl[a]	exptl[b]	calcd[c]	assgnt (C_s)[d]	
3490	3080 br	3404(181)[998]	$\nu_1(A')$, $\nu(O{-}H)$	
1697	1681(4) 1668(4)	1725(3)[414]	$\nu_2(A')$, $\nu_{as}(NO_2) + \delta(N{-}O{-}H)$	
1343	1301(4) 1291(35) 1289 sh	1414(7)[222]	$\nu_3(A')$, $\delta(N{-}O{-}H)$	
1311	1247(6)	1327(22)[191]	$\nu_4(A')$, $\nu_s(NO_2) - \delta(N{-}O{-}H)$	
902	953(4) 926(14)	933(12)[141]	$\nu_5(A')$, $\nu(N{-}O_H) + \delta(NO_2)$	
767	n.o.	795(<0.1)[2]	$\nu_{14}(A'')$, $\rho_w(NO_3)$	
479	706(<1)	750(<1)[91]	$\nu_{15}(A'')$, $\rho_w(N{-}O{-}H)$	
660	698(<1) 686(11)	677(4)[6]	$\nu_6(A')$, $\nu(N{-}O_H) - \delta(NO_2)$	
597	638(1) 624(10)	622(3)[1]	$\nu_7(A')$, $\delta(O{-}N{-}O_H) + \rho_r(NO_2)$	
	529(100)	550(21)[174]	$\nu_8(A')$, $\nu(Xe{-}F_t)$ – small $\nu(Xe{-}F_H)$	
	468(29) 458(47)	480(30)[109]	$\nu_9(A')$, $\nu(Xe{-}F_H)$ + small $\nu(Xe{-}F_t)$	
	294(2)	238(<1)[36]	$\nu_{10}(A')$, $\delta(XeF_2)$i.p. + $\rho_r(HNO_3)$	
	238(1)	203(<1)[11]	$\nu_{16}(A'')$, $\delta(XeF_2)$o.o.p. + $\rho_w(N{-}O{-}H)$	
	159(5)	144(<1)[8]	$\nu_{11}(A')$, $\delta(XeF_2)$i.p. – $\rho_r(HNO_3)$	
	130(32)		lattice mode	
	106(11) 101(12)	107(2)[<1]	$\nu_{12}(A')$	strongly coupled deformation modes
	70(2)	72(2)[<1]	$\nu_{13}(A')$	
		42(<1)[1]	$\nu_{17}(A'')$	
		32(<1)[<0.1]	$\nu_{18}(A'')$	

[a] Infrared spectrum of monomeric HNO_3 in a N_2 matrix (6−10 K); taken from ref 42. [b] The Raman spectrum was recorded in a FEP sample tube at −160 °C using 1064-nm excitation; relative Raman intensities are given in parentheses. Abbreviations denote shoulder (sh) and broad (br). A band observed at 496(24) cm^{-1} was assigned to the $\nu_1(\Sigma_g^+)$ band of free XeF_2. [c] B3LYP/aug-cc-pVTZ(-PP). Values in parentheses denote Raman intensities (Å^4 u^{-1}), and those in square brackets denote infrared intensities (km mol^{-1}). [d] Subscripts indicate the fluorine atom hydrogen-bonded (F_H) to HNO_3 and the terminal fluorine atom on Xe (F_t). The abbreviations denote symmetric (s), asymmetric (as), stretch (ν), bend (δ), rock (ρ_r), wag (ρ_w), in-plane bend (i.p.), and out-of-plane bend (o.o.p.). The in-plane and out-of-plane mode descriptions are relative to the HNO_3 plane.

$XeF_2 \cdot HNO_3$ is provided in Table S15 (Supporting Information) and predicts that each gas-phase Raman- and infrared-active band of $XeF_2 \cdot HNO_3$ is split, as a result of vibrational-coupling within the crystallographic unit cell (D_{2h} symmetry), into a maximum of four Raman-active (A_g, B_{1g}, B_{2g}, and B_{3g}) and four infrared-active (A_u, B_u, B_{2u}, and B_{3u}) components. Three components are observed for the $\delta(N{-}O{-}H)$ mode, six modes including that of $\nu(Xe{-}F_H)$ (vide infra) are split into two components, and no splittings are resolved for the remaining eight modes in the Raman spectrum (Table 6).

Hydrogen-bonding between the OH group of HNO_3 and one of the fluorine ligands of XeF_2 results in loss of the center of symmetry in XeF_2 and in the intense Raman bands at 529 cm^{-1} and at 458, 468 cm^{-1} that are assigned to $\nu(XeF_t)$ (calcd 550 cm^{-1}) and $\nu(XeF_H)$ (calcd 480 cm^{-1}), respectively. Splitting of the low-frequency mode arises from vibrational coupling within the crystallographic unit cell. Unlike the Xe−F stretching modes of free XeF_2 ($\nu_1(\Sigma_g^+) = 497$ cm^{-1}, $\nu_2(\Pi) = 213.2$ cm^{-1}, $\nu_3(\Sigma_u^+) = 555$ cm^{-1}),[43] the $\nu(XeF_t)$ and $\nu(XeF_H)$ modes in adducted XeF_2 are very weakly coupled. The magnitude of the $\nu(XeF_t)$ and $\nu(XeF_H)$ frequency difference (66 cm^{-1}) is approximately half of the average ranges observed for XeF_2 homoleptically coordinated to metal cations,[44,45] where the higher frequency bands range from 544 to 584 cm^{-1} and are assigned to $Xe{-}F_t$ stretching modes and the lower frequency bands range from 411 to 479 cm^{-1} and are assigned to bridging $Xe{-}F_b$ stretching modes. The observed difference is well reproduced by the calculations (70 cm^{-1}).

The frequencies occurring between 624 and 3080 cm^{-1} are associated with HNO_3 modes and are not coupled to the XeF_2 modes of the adduct. With the exception of ν_3 and ν_4 observed at 1291 and 1247 cm^{-1}, the mode descriptions are the same as those of matrix-isolated HNO_3. The two modes that are the most affected upon adduct formation are $\nu(OH)$ and $\rho_w(NOH)$, which shift to lower frequency by 410 cm^{-1} and to higher frequency by 227 cm^{-1}, respectively, as a result of H-bonding. Significant shifts are also calculated for these modes (−306 and +264 cm^{-1}, respectively). The shifts to lower frequency for the stretch and to higher frequency for the wag are consistent with a H···F interaction that is stronger than the intramolecular H···O interaction in matrix-isolated HNO_3. The shifts to low (ν_2) and high (ν_{5-} ν_7) frequencies are also reproduced by the calculations. Although derived from ν_3 and ν_4 of HNO_3, the shifts for ν_3 and

---

(43) Argon, P. A.; Begun, G. M.; Levy, H. A.; Mason, A. A.; Jones, C. G.; Smith, D. F. *Science* **1963**, *139*, 842–843.

(44) Tavčar, G.; Tramšek, M.; Bunič, T.; Benkič, P.; Žemva, B. *J. Fluorine Chem.* **2004**, *125*, 1579–1584.

(45) Tramšek, M.; Žemva, B. *J. Fluorine Chem.* **2006**, *127*, 1275–1284.

Table 7. Experimental and Calculated Vibrational Frequencies for $XeF_2 \cdot N_2O_4$

frequencies, cm^{-1}				
N_2O_4	$XeF_2 \cdot N_2O_4$			
exptl[a,b]	exptl[a,c]	calcd (model A)[d,e]	calcd (model B)[d,f]	assgnt (C_1)[g]
	n.o.	1811(<1)[711]	1811(<1)[669]	$\nu(NO_A) + \nu(NO_A') - (\nu(NO_B) + \nu(NO_B'))$
1726(21)	1711(6)	1780(12)[<1]	1777(13)[6]	$\nu(NO_A) + \nu(NO_B') - (\nu(NO_B) + \nu(NO_A'))$
1385(36) 1375(1)	1394(7)	1444(24)[<1]	1442(28)[<1]	$\nu(NO_A) + \nu(NO_A') + \nu(NO_B) + \nu(NO_B')$
	n.o.	1302(<1)[435]	1299(<1)[556]	$\nu(NO_A) + \nu(NO_B) - (\nu(NO_A') + \nu(NO_B'))$
812(30)	817(16)	852(25)[<1]	851(34)[<0.1]	$\delta(NO_2) + \delta(NO_2')$
	n.o.	764(<1)[248]	761(<1)[313]	$\delta(NO_2) - \delta(NO_2')$
678(4)	691(<1)	706(<1)[<1]	702(<1)[<0.1]	$\rho_w(NO_2) - \rho_w(NO_2')$
	n.o.	547(6)[238]	546(<1)[271]	$\nu(XeF) - \nu(XeF)$
	509(100)	504(43)[22]	507(49)[1]	$\nu(XeF) + \nu(XeF)$
499(22)		502(7)[<0.1]	488(8)[<0.1]	$\rho_r(NO_2) - \rho_r(NO_2')$
	n.o.	453(<1)[28]	447(<0.1)[13]	$\rho_w(NO_2) + \rho_w(NO_2')$
285(97) 281(100)	296(58)	300(38)[<1]	297(61)[<1]	$\nu(N–N)$
		232(<0.1)[<1]	227(<0.1)[<0.1]	$\rho_r(NO_2) + \rho_r(NO_2') +$ small $\delta(XeF_2)$
	n.o.	214(<1)[17]	208(<0.1)[21]	$\rho_r(NO_2) + \rho_r(NO_2') -$ small $\delta(XeF_2)$
		207(<0.1)[11]	206(<0.1)[13]	$\rho_t(NO_2) - \rho_t(NO_2') +$ small $\delta(XeF_2)$
	n.o.	102(<0.1)[<0.1]	94(<0.1)[<0.1]	$\rho_t(NO_2) - \rho_t(NO_2')$
121(3) 79(50)	98(10) 71(7)			lattice modes
		80(4)[<1]	45(5)[<0.1]	$\delta(XeF_2) + \rho_r(N_2O_4)$
		47(1)[<1]	40(4)[<0.1]	$\rho_t(NO_2) - \rho_t(NO_2') + \rho_t(XeF_2)$
		43(2)[<1]	23(<1)[<0.1]	$\rho_r(XeF_2) + \rho_r(N_2O_4)$
		15(<1)[<1]	10(<1)[<0.1]	$\rho_r(XeF_2) - \rho_r(N_2O_4)$
		13(3)[<0.1]	4(2)[<0.1]	$\rho_t(XeF_2) + \rho_t(N_2O_4)$

[a] Raman spectra of solid N_2O_4 and $XeF_2 \cdot N_2O_4$ were recorded in FEP sample tubes at −160 °C using 1064-nm excitation; relative Raman intensities are given in parentheses. Abbreviations denote shoulder (sh) and not observed (n.o.). [b] A combination band was also observed at 1337(10) cm^{-1}. [c] Modes associated with uncomplexed N_2O_4 were observed at 1726(41), 1385(69), 1375(1), 1337(20), 812(55), 678(7), 498(43), 284(176), 281(181), 121(8), and 79(96) cm^{-1}. A combination band was also observed at 1354(8) cm^{-1}. [d] B3LYP/aug-cc-pVTZ(-PP). Values in parentheses denote Raman intensities ($Å^4\ u^{-1}$), and those in square brackets denote infrared intensities (km mol^{-1}). [e] Calculated frequencies correspond to the calculated geometry in Figure 5b. [f] Calculated frequencies correspond to the calculated geometry in Figure 5c. [g] Abbreviations denote stretch (ν), bend (δ), wag (ρ_w), twist (ρ_t), and rock (ρ_r). Bond elongations and angle openings are denoted by plus (+) signs, and bond contractions and angle closings are denoted by minus (−) signs. The labels A (A′) and B (B′) denote oxygen atoms that are coordinated to the same N (N′) atom of $O_2N–N'O_2$, where A (B) and A′ (B′) are cis to one other.

ν_4 cannot be directly compared because the contributions to these coupled modes differ significantly from those of matrix-isolated HNO_3.

2.8.3. $XeF_2 \cdot N_2O_4$. The vibrational modes of $XeF_2 \cdot N_2O_4$ were assigned using the frequencies calculated for models A (Figure 5b) and B (Figure 5c) under C_1 symmetry. For each model, a total of 21 fundamental vibrations belonging to A irreducible representations are expected, all of which are Raman and infrared active. Because the unit cell (C_i symmetry) is occupied by only one $XeF_2 \cdot N_2O_4$ molecule having C_1 site symmetry, the Raman bands are not factor-group split.

Models A and B have very similar calculated frequencies and relative intensities (Table 7 and Table S7 in the Supporting Information), showing that the two coordination modes observed experimentally would give rise to nearly coincident spectra. A notable difference occurs for the mode assigned to $\nu_{as}(XeF_2)$, which is predicted to have a moderate intensity in the Raman spectrum for model A (Figure 5b). Only the seven bands that are predicted to be intense in the Raman spectra of both models were observed experimentally.

Only one XeF_2 stretching band is observed at 509 cm^{-1}, which is only 13 cm^{-1} higher in frequency than $\nu_1(\Sigma_g^+)$ of free XeF_2 (497 cm^{-1}),[43] indicating that the interactions with N_2O_4 are weak and that the local $D_{\infty h}$ symmetry and the inversion center of XeF_2 are retained at the local symmetry level. Moreover, none of the N_2O_4 modes of the adduct are significantly shifted with respect to those of free N_2O_4[46] (Table 7 and Tables S7 and S12 in the Supporting Information). Despite the weak interactions between XeF_2 and N_2O_4, the local $D_{\infty h}$ (XeF_2) and D_{2h} (N_2O_4) symmetries are retained in the centrosymmetric unit cell of $XeF_2 \cdot N_2O_4$. Consequently, the formally Raman inactive *ungerade* modes corresponding to those of free N_2O_4 and XeF_2 are also not observed in the experimental spectrum of $XeF_2 \cdot N_2O_4$ (Table 7). Overall, and unlike $XeF_2 \cdot HNO_3$, the XeF_2 portion of the $XeF_2 \cdot N_2O_4$ Raman spectrum is consistent with a weakly bound molecular addition compound (also see Computational Results).

2.9. Computational Results. The electronic structures of $FXeONO_2$, $XeF_2 \cdot HNO_3$, $XeF_2 \cdot N_2O_4$, $BrONO_2$, $ClONO_2$, $Xe(ONO_2)_2$, NO_2^+, $FXeON(O)F^+$, and $FXeFNO_2^+$ were optimized using the B3LYP, PBE1PBE, and MP2 methods and the aug-cc-pVTZ(-PP) basis sets, resulting in stationary points with all frequencies real (Tables 5−7 and Tables S3−S7, S14, and S16 in the Supporting Information; also see Experimental Section). The compounds XeF_2, HNO_3, and N_2O_4 were also calculated for comparison (Tables S8−S12, Supporting Information). Values referred to in the following discussion were calculated at the B3LYP/aug-cc-PVTZ(-PP) level of theory. The

---

(46) Andrews, B.; Anderson, A. *J. Chem. Phys.* **1981**, *74*, 1534–1537.

PBE1PBE and MP2 values are given in Tables S3−S12, S14, and S16 of the Supporting Information.

2.9.1. Geometries. (a) $FXeONO_2$. The $FXeONO_2$ geometry optimized to C_s symmetry (Figure 1b) starting from the crystallographic geometry or from a C_{2v} symmetric $FXeO_2N{=}O$ molecule having a bidentate nitrate group bonded to xenon and is in very good agreement with the experimental geometry, underscoring that the $FXeONO_2$ molecule is well isolated in the crystal structure. This is particularly true for the bond angles, which are often most affected by crystal packing. There is excellent agreement between the calculated (2.148 Å) and experimental (2.126(4) Å) Xe−O and Xe−F bond lengths (2.018 and 1.992(4) Å, respectively). The calculations also accurately reproduce the slight difference between the terminal N−O bond lengths, which are 1.200 Å for the N−O bond anti to xenon and 1.211 Å for the N−O bond syn to xenon (experimental, 1.199(6) and 1.224(6) Å, respectively). Similarly, all of the calculated angles are in good agreement with the experimental values (Table 3 and Table S3 in the Supporting Information).

(b) $Xe(ONO_2)_2$. Although $Xe(ONO_2)_2$ was not synthesized in the present work, the energy-minimized geometry was calculated (Figure S4 and Table S16, Supporting Information). Both the *syn*- (C_s) and *anti*- (C_{2v}) isomers of $Xe(ONO_2)_2$ were used as starting geometries, but both geometries optimized to a lower energy C_1 geometry, with a dihedral angle between the two NO_3 planes of 108.9°. The calculated geometric parameters for $FXeONO_2$ and $Xe(ONO_2)_2$ are very similar, with the Xe−O bond length being slightly longer for $Xe(ONO_2)_2$ (2.168 Å) than for $FXeONO_2$ (2.148 Å). The Xe−O−N angle (115.7°) is very similar to that in $FXeONO_2$ (116.0°), with very similar angles around nitrogen (Table S16).

(c) $XeF_2\cdot HNO_3$. The energy-minimized geometry of $XeF_2\cdot HNO_3$ is a planar structure, in agreement with the experimental structure (see X-ray Crystallography). The experimental $Xe{-}F_t$, $Xe{-}F_H$, and N−O bond lengths, as well as their associated bond angles, were accurately reproduced by the calculations, whereas some discrepancies occurred for the intramolecular contacts. The difference between the experimental and calculated Xe(1)···O(3) contact distances (3.317(1) and 3.034 Å, respectively) is likely attributable to weak intermolecular contacts from neighboring XeF_2 and HNO_3 molecules within the crystal lattice (Table 3). Such contacts, which are not taken into account by the present model, are expected to weaken the Xe(1)···O(3) contact. The calculated O−H (1.016 Å) and H···F (1.520 Å) distances differ significantly from the experimental values of 0.83(2) and 1.86(2) Å, which is likely attributable to the uncertainty in the location of the hydrogen atom in the experimental electron density map (see X-ray Crystallography). Although the experimental and calculated O−H and H···F distances differ significantly from experiment, the calculated O(2)···F(2) distance (2.536 Å) is in reasonable agreement with the experimental distance (2.690(1) Å).

(d) $XeF_2\cdot N_2O_4$. An attempt to calculate the structure depicted in Figure 5a from the crystal structure coordinates failed to optimize. Therefore, three simplified models corresponding to the three coordination modalities observed in the crystal structure of $XeF_2\cdot N_2O_4$ (Figure 5a) were considered. The monodentate model optimized to the bidentate geometry shown in Figure 5b. The bidentate models, A and B, were shown to correspond to local minima (Figure 5b,c), with calculated bond lengths, bond angles, and contact distances that are in reasonable agreement with those of the experimental structure. Unlike the symmetric arrangement of N_2O_4 molecules found in the crystal structure (Figure 5a), both optimized structures (Figure 5b,c) are asymmetric. The vibrational frequencies of both calculated structures proved instrumental in assigning the Raman spectrum of solid $XeF_2\cdot N_2O_4$ (see Raman Spectroscopy).

2.9.2. Natural Bond Orbital (NBO) Analyses. The NBO analyses were carried out for the MP2- and B3LYP-optimized gas-phase geometries of $FXeONO_2$, $XeF_2\cdot HNO_3$, $XeF_2\cdot N_2O_4$, $Xe(ONO_2)_2$, XeF_2, HNO_3, and N_2O_4. The NBO results are given in Tables S8 and S17 (Supporting Information). The MP2 and B3LYP results are similar; only the MP2 results are discussed here.

(a) $FXeONO_2$ and $Xe(ONO_2)_2$. As with the geometric parameters, the charges, valencies, and bond orders were found to be very similar for $FXeONO_2$ and $Xe(ONO_2)_2$ and are not discussed in detail for the latter compound. The charge on Xe is somewhat higher for $FXeONO_2$ (1.15) than for $Xe(ONO_2)_2$ (1.08), indicative of the greater electron-withdrawing ability of the fluorine ligand when compared with that of the nitrate ligand. This is corroborated by comparison with the xenon charge in XeF_2 (1.20). The negative charges on the fluorine (−0.59) and the oxygen directly bonded to xenon (−0.59) of $FXeONO_2$ are essentially equal to the fluorine charges in XeF_2 (−0.60). The Xe−F (0.31) and Xe−O (0.36) bond orders of $FXeONO_2$ and XeF_2 (0.34) are also very similar. In the case of the Xe−O−N bridge, the ratio of the terminal N(1)−O(2,3) bond orders (1.21) to that of N(1)−O(1) (0.79) is ca. 1.5, which is in accordance with nearly equal weightings of dominant valence bond structures I and II. The individual charges of the NO_3 group are 0.66 (N), −0.28 (O_A), −0.34 (O_S), and −0.56 (O bonded to Xe). The greater negative charge on the oxygen syn to the FXeO− group suggests a significant interaction with the positive xenon center which polarizes the NO_2 group and leads to more negative charge on the syn oxygen. The calculated $Xe\cdots O_S$ distance is 2.935 Å, which is significantly less than the sum of the van der Waals radii for xenon and oxygen (3.68 Å) and is consistent with such an interaction. The NBO analysis also shows that there is a small $Xe\cdots O_S$ bond order (0.02). The overall charge of the NO_3 group (−0.56) and the charge on Xe (1.15) are also consistent with nearly equal contributions from structures I and II.

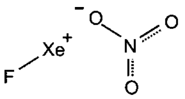

I

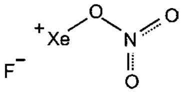

II

(b) $XeF_2\cdot HNO_3$ and $XeF_2\cdot N_2O_4$. The charges and valencies calculated for HNO_3 and N_2O_4 in their XeF_2 adducts are similar to those calculated for free HNO_3 and N_2O_4. In the case of $XeF_2\cdot HNO_3$, the H···F bond order (0.04) is somewhat greater than the Xe···O bond order (0.01), with their small values being consistent with the weak interactions observed in the crystal structure. The negative charge on F(1) (−0.57) is somewhat diminished by H-bond formation relative to that of F(2) (−0.63).

The small bond orders calculated for the O···Xe interactions in $XeF_2\cdot N_2O_4$ (0.02 for models A and B) are in accordance with the X-ray crystal structure, where only very weak Xe···O interactions were observed (3.435(4)−4.180(4) Å, see X-ray Crystallography). The xenon charges of $XeF_2\cdot HNO_3$ and $XeF_2\cdot N_2O_4$ (A and B) (1.23 and 1.22, 1.21 respectively) are essentially unchanged relative to that of XeF_2 (1.20), which is also consistent with a molecular addition compound.

3. Conclusions

The synthesis and structural characterization of $FXeONO_2$ confirms the ability of the nitrate ligand to stabilize the +2 oxidation state of xenon. The present synthesis of $FXeONO_2$ from $[FXeOXeFXeF][AsF_6]$ and NO_2F is the only synthetic route presently known that yields isolable amounts of $FXeONO_2$ and provides an interesting synthetic application of the $Xe_3OF_3^+$ cation, the only known oxide fluoride cation of xenon(II). Raman and NMR spectroscopic studies, as well as an X-ray crystallographic study, show that $FXeONO_2$ is strongly covalently bound to xenon, which is corroborated by gas-phase quantum-chemical calculations. The mechanism leading to the formation of $FXeONO_2$ has been explored using ^{18}O-labeled $[FXe^{18}OXeFXeF][AsF_6]$. The exclusive occurrence of $FXe^{16}ON(^{16}O^{18}O)$ as the labeled product is consistent with the formation of $^{18}O(XeF)_2$ and $FXeON(O)F^+/FXeFNO_2^+$ as reaction intermediates. The absence of $^{16/18}O$ isotopic scrambling among the oxygen sites of $FXeONO_2$ was confirmed by factor-group analyses of the 16 isotopomeric crystallographic unit cells that result from *syn-*/*anti*-isomerization, $FXe^{16}ON(^{16}O_A{}^{18}O_S)$/$FXe^{16}ON(^{16}O_S{}^{18}O_A)$, among the four $FXeONO_2$ molecules of the unit cell. A second pathway for oxygen exchange between $FXe^{16}ON(^{16}O^{18}O)$ and $N^{16}O_2^+$ led to the formation of a minor amount of $^{16}ON^{18}O^+$.

The X-ray crystallographic and Raman spectroscopic study of the $XeF_2 \cdot HNO_3$ adduct is only the second known example of a H-bonded adduct of XeF_2, while the molecular addition compound, $XeF_2 \cdot N_2O_4$, shows that N_2O_4 interacts in a bidentate fashion with the xenon atom through two oxygen atoms bound to two different nitrogen atoms or through two oxygen atoms bound to the same nitrogen atom. Computational studies have provided the geometric parameters of the presently unknown $Xe(ONO_2)_2$ molecule and have accurately reproduced the experimental geometric parameters and trends in the vibrational frequencies of $FXeONO_2$, $XeF_2 \cdot HNO_3$, and $XeF_2 \cdot N_2O_4$. The calculated ΔH and ΔG values at 298.15 and 195.15 K show that the gas-phase decompositions of $FXeONO_2$ and $Xe(ONO_2)_2$ are spontaneous for all reaction channels considered and are consistent with the experimental decomposition products. Although the gas-phase thermochemical parameters for the reaction of $FXeONO_2$ and AsF_5 to form $XeONO_2^+$ and AsF_6^- is very endothermic and nonspontaneous, the low-temperature experimental reaction of $FXeONO_2$ with liquid AsF_5 is spontaneous, forming $[NO_2][AsF_6]$, Xe, and O_2. The sought-after $[XeONO_2][AsF_6]$ salt was not observed as an intermediate by low-temperature Raman spectroscopy. The findings are consistent with volume-based thermodynamic calculations which indicate that, while the reaction of $FXeONO_2$ and AsF_5 to form $[XeONO_2][AsF_6]$ is spontaneous under standard conditions, the salt is unstable with respect to the observed decomposition products.

4. Experimental Section

4.1. Apparatus and Materials. All manipulations were carried out under anhydrous conditions using glass and metal vacuum lines as previously described.[44,47] Sulfuryl chloride fluoride (SO_2ClF, Allied Chemical)[29] and anhydrous HF (Harshaw Chemicals Co.)[49] were purified using the standard literature methods. Nitrogen dioxide (Matheson) was purified by pressurizing a sample with high-purity O_2 (Canadian Liquid Air, zero grade) and allowing it to stand at room temperature for 24 h, followed by removal of unreacted O_2 by pumping at −196 °C and three thawing, refreezing (−196 °C), and pumping cycles. Red, fuming nitric acid (90%, Fischer Scientific Co.) was dried in 30% oleum (1:4 v/v), followed by static vacuum distillation at 0 °C[50] into an intermediate glass vessel sealed with a 4-mm J. Young glass/Teflon stopcock. Dinitrogen pentoxide was prepared by dehydration of 100% HNO_3 over P_4O_{10} as previously described.[51] Sodium nitrite (BDH Chemical, ≥97%) and ^{15}N-enriched $NaNO_2$ (98+ atom % ^{15}N, Isotec) were dried under dynamic vacuum at 150 °C for 24 h and used without further purification. Arsenic pentafluoride[52] and XeF_2[53] were prepared as previously described and used without further purification. The syntheses of $[Xe_3OF_3][AsF_6]$ and $[Xe_3{}^{18}OF_3][AsF_6]$ are described in ref 20. Both NO_2F[54] and $^{15}NO_2F$[55] were prepared according to the literature methods, with some modifications as described in the Supporting Information.

4.2. Syntheses of $FXeONO_2$, $FXe^{16}ON(^{16}O^{18}O)$, and $FXeO^{15}NO_2$. In a typical synthesis, ca. 100 mg of $[Xe_3OF_3][AsF_6]$ ($[Xe_3{}^{18}OF_3][AsF_6]$) was synthesized as previously described[20] in a $^1/_4$-in. o.d. FEP reaction vessel outfitted with a Kel-F valve. The reaction vessel also had a section of $^1/_4$-in. o.d. FEP tubing fused to it, forming a side arm that was bent to form an h-shaped reactor. The h-shaped reactor and a $^1/_4$-in. o.d. FEP transfer vessel fitted with a Kel-F valve were connected by means of 45° SAE compression fittings to a three-way FEP connector. A nickel vessel outfitted with a 316 stainless steel valve and containing NO_2F ($^{15}NO_2F$) was connected to the remaining port of the three-way connector by means of a $^1/_4$-in. stainless steel Swagelok Ultratorr union fitted with Viton O-rings. All connections and the FEP reaction vessels were passivated with F_2 for several hours prior to use. The nickel NO_2F sample vessel was cooled to −78 °C, and a portion of NO_2F was condensed into a second $^1/_4$-in. o.d. FEP vessel at −196 °C, followed by warming to −78 °C to control the amount of NO_2F added to $[Xe_3OF_3][AsF_6]$. The NO_2F in the auxiliary vessel (−78 °C) was then condensed onto $[Xe_3OF_3][AsF_6]$ at −196 °C, followed by warming the reaction mixture to −50 °C, where, after 5 h, the solid slowly changed from a magenta or red-orange color to a white suspension in excess liquid NO_2F. Excess NO_2F was removed under vacuum at −110 °C to yield a white, microcrystalline, solid mixture of $FXeONO_2$, XeF_2, and $[NO_2][AsF_6]$. Sulfuryl chloride fluoride (ca. 0.75 mL) was then condensed onto the mixture at −196 °C. The solution was warmed to −30 °C and agitated for several seconds to effect dissolution of $FXeONO_2$ and XeF_2. The solid was allowed to settle (ca. 1 min), and the supernatant was then decanted into the side arm of the reaction vessel at −78 °C. After the solid had settled to the bottom of the side arm, the supernatant was decanted into the main tube of the reactor, and the process was repeated. Longer extraction times (ca. 5−10 min) and/or more agitation in attempts to improve product yield resulted in partial $[NO_2][AsF_6]$ extraction, thereby contaminating the final product. The main portion of the reactor, containing $[NO_2][AsF_6]$, was removed by heat-sealing it off under dynamic vacuum, and

---

(47) Casteel, W. J., Jr.; Kolb, P.; LeBlond, N.; Mercier, H. P. A.; Schrobilgen, G. J. *Inorg. Chem.* **1996**, *35*, 929–942.
(48) Casteel, W. J., Jr.; Dixon, D. A.; Mercier, H. P. A.; Schrobilgen, G. J. *Inorg. Chem.* **1996**, *35*, 4310–4322.
(49) Emara, A. A. A.; Schrobilgen, G. J. *Inorg. Chem.* **1992**, *31*, 1323–1332.
(50) Morton, J. R.; Wilcox, H. W. *Inorg. Synth.* **1953**, *4*, 52–53.
(51) Schenk, P. W. In *Handbook of Preparative Inorganic Chemistry*; Brauer, G., Ed.; Academic Press: New York, 1963; Vol. 1, pp 489−491.
(52) Emara, A. A. A.; Lehmann, J. F.; Schrobilgen, G. J. *J. Fluorine Chem.* **2005**, *126*, 1373–1376.
(53) Mercier, H. P. A.; Sanders, J. C. P.; Schrobilgen, G. J.; Tsai, S. S. *Inorg. Chem.* **1993**, *32*, 386–393.
(54) Faloon, A. V.; Kenna, W. B. *J. Am. Chem. Soc.* **1951**, *73*, 2937–2938.
(55) Aynsley, E. E.; Hetherington, G.; Robinson, P. L. *J. Chem. Soc.* **1954**, 1119–1124.

the $FXeONO_2/XeF_2$ mixture was dried under dynamic vacuum at −78 °C and stored at that temperature until studied by Raman spectroscopy.

4.3. Reactions of XeF_2 with HNO_3. On a glass vacuum line, 100% HNO_3 (0.1047 g, 1.661 mmol) was condensed into a $^1/_4$-in. o.d. FEP reactor fitted with a Kel-F valve. Sulfuryl chloride fluoride (ca. 1.5 mL) was then condensed onto the sample at −196 °C. The solution was frozen at ca. −145 °C inside a drybox, and XeF_2 (0.1406 g, 0.831 mmol) was then added to the reaction vessel. The mixture was warmed to −30 °C and agitated for 1 h, after which the solvent was removed under vacuum at −78 °C to give white, microcrystalline $XeF_2 \cdot HNO_3$.

4.4. Attempted Syntheses of $Xe(ONO_2)_2$ and $FXeONO_2$ by Reaction of XeF_2 and $[XeF][AsF_6]$ with N_2O_5. Dinitrogen pentoxide (ca. 0.100 g, 0.93 mmol) was sublimed into a $^1/_4$-in. o.d. FEP reactor fitted with a Kel-F valve on a glass vacuum line. Liquid SO_2ClF was then condensed onto the sample at −196 °C (ca. 1.5 mL), followed by pressurizing the reaction vessel with 1 atm of dry nitrogen. The reactor was transferred into a drybox, and XeF_2 (0.2351 g, 1.389 mmol) or $[XeF][AsF_6]$ (0.3140 g, 0.926 mmol) was added to the frozen mixture (−140 °C) and removed to a −78 °C dry ice/acetone bath. The mixture of XeF_2/N_2O_5 was gradually warmed to 0 °C to effect dissolution and monitored by low-temperature Raman spectroscopy but showed no sign of reaction after 24 h. Further warming to 10−15 °C for 2 days also showed no sign of reaction.

The solid mixture of $[XeF][AsF_6]/N_2O_5$ formed orange and white clumps under SO_2ClF at −78 °C. When warmed to −30 °C, N_2O_5 appeared to dissolve, and further reaction took place. After ca. 30 min, the orange color dissipated, at which time the sample was cooled to and stored at −78 °C until a low-temperature Raman spectrum could be recorded.

4.5. Synthesis of $XeF_2 \cdot N_2O_4$. Xenon difluoride (0.1510 g, 0.892 mmol) was added to a $^1/_4$-in. o.d. FEP reactor fitted with a Kel-F valve inside the drybox. Liquid N_2O_4 was condensed onto the sample at −78 °C (ca. 1.5 mL), followed by pressurization with 1 atm of dry nitrogen. The reactor was warmed to 10 °C to effect complete dissolution of XeF_2 and initially gave a pale brown solution. Cooling to −10 °C resulted in precipitation of the $XeF_2 \cdot N_2O_4$ as a white solid. Adduct formation was verified by low-temperature Raman spectroscopy of the compound in the presence of frozen N_2O_4.

4.6. Raman Spectroscopy. The low-temperature (−160 °C) Raman spectra of $FXeONO_2$, $XeF_2 \cdot HNO_3$, and $XeF_2 \cdot N_2O_4$ were recorded on a Bruker RFS 100 FT Raman spectrometer using 1064-nm excitation and a resolution of 1 cm^{-1} as previously described.[56] Spectra were recorded using a laser power of 300 mW and a total of 600 scans. The white solid mixture of $FXeONO_2$, XeF_2, and $[NO_2][AsF_6]$ resulting from the reaction of $[Xe_3OF_3][AsF_6]$ with NO_2F was recorded. Another spectrum of a mixture of $FXeONO_2$ and XeF_2 extracted with SO_2ClF at −35 °C was recorded after removal of SO_2ClF under vacuum at −78 °C. The spectrum of $XeF_2 \cdot HNO_3$ was recorded on a sample of XeF_2 and HNO_3 that had been allowed to react in a 1:1 ratio in SO_2ClF at −30 °C for 1 h and was isolated by pumping off the solvent under vacuum at −78 °C. The spectrum of $XeF_2 \cdot N_2O_4$ was recorded on a sample of XeF_2 frozen in excess N_2O_4 solution.

4.7. Nuclear Magnetic Resonance Spectroscopy. 4.7.1. NMR Sample Preparation. Samples for NMR spectroscopy were prepared in situ by carrying out the scaled-down versions of the previously described reactions in FEP NMR tubes. The NMR tubes were constructed from 4-mm o.d. FEP tubing fused to 5-cm lengths of $^1/_4$-in. o.d. × $^1/_{32}$-in. wall FEP tubing which, in turn, were flared and fitted to Kel-F valves with compression fittings. In the case of $FXeONO_2$, samples were prepared by extracting a mixture of $FXeONO_2$ and XeF_2 with SO_2ClF into a 4-mm o.d. FEP side arm that was fused to a $^1/_4$-in. o.d. FEP reaction vessel and functioned as an NMR sample tube (see Syntheses of $FXeONO_2$, $FXe^{16}ON(^{16}O^{18}O)$, and $FXeO^{15}NO_2$). In all cases, the NMR sample tubes were frozen at −196 °C and heat-sealed under dynamic vacuum.

4.7.2. NMR Instrumentation and Spectral Acquisition. Nuclear magnetic resonance spectra were recorded unlocked (field drift <1 Hz h^{-1}) on a Bruker DRX-500 spectrometer equipped with a 11.744-T cryomagnet and a 5-mm broad-band inverse probe. The low-field ^{19}F and ^{129}Xe NMR spectra of $FXeO^{15}NO_2$ in SO_2ClF were also recorded on a Bruker AV-300 spectrometer equipped with a 7.0463-T cryomagnet using a 5-mm broad-band probe for ^{129}Xe and a 5-mm $^1H/^{13}C/^{19}F/^{31}P$ combination probe for ^{19}F.

The ^{19}F NMR spectra were recorded at 470.592 (282.363 at 7.0463 T) MHz in 64K memories, with a spectral width setting of 24 (28) kHz, yielding a data point resolution of 0.36 (0.43) Hz/data point and acquisition times of 1.39 (1.16) s. A relaxation delay of 0.1 s was applied, and 1500−2000 transients were typically accumulated using a pulse width of 2.5 (6.0) μs, corresponding to a bulk magnetization tip angle, θ, of approximately 90°. A line-broadening of 0.1 Hz was used in the exponential multiplication of the free induction decays prior to Fourier transformation.

The ^{129}Xe NMR spectra were recorded at 138.857 (83.307 at 7.0463 T) MHz in 32 (16)K memories, with a spectral width setting of 100 (33.3) kHz, yielding a data point resolution of 3.05 (2.03) Hz/data point and acquisition times of 0.16 (0.25) s. A relaxation delay of 0.1 s was applied, and 50 000−100 000 transients were typically accumulated using a pulse width of 12.2 (6.0) μs, corresponding to a bulk magnetization tip angle, θ, of approximately 90°. A line broadening of 5−20 Hz was used in the exponential multiplication of the free induction decays prior to Fourier transformation.

The ^{14}N (^{15}N) NMR spectra were recorded at 36.141 (50.678) MHz in 16 (32)K memories, with a spectral width setting of 29.0 (16.7) kHz, yielding a data point resolution of 1.76 (0.51) Hz/data point and acquisition times of 0.28 (0.98) s. A relaxation delay of 0.05 (180) s was applied, and 100 000 (170) transients were accumulated using a pulse width of 13.8 (28.0) μs, corresponding to a bulk magnetization tip angle, θ, of approximately 90°. A line broadening of 10 (5) Hz was used in the exponential multiplication of the free induction decays prior to Fourier transformation.

The $^{14/15}N$, ^{19}F, and ^{129}Xe NMR spectra were referenced externally at 30 °C to samples of neat CH_3NO_2, $CFCl_3$, and $XeOF_4$, respectively. The chemical shift convention used is that a positive (negative) sign denotes a chemical shift to high (low) frequency of the reference compound.

4.8. X-ray Crystallography. 4.8.1. Crystal Growth. All crystals were grown at low temperatures in one arm of a $^1/_4$-in. o.d. FEP T-shaped reactor consisting of a reaction tube heat fused to a side arm and fitted with a Kel-F valve as previously described.[57] The main arm of the reaction vessel containing the colorless solution was placed inside the precooled glass dewar of a crystal growing apparatus, and the temperature of the dewar and contents was slowly lowered to induce slow crystal growth.[57] The crystals were isolated by decanting the solvent under dry nitrogen, at the temperature achieved at the end of crystal growth, into the side arm of the FEP vessel, which was initially immersed in a dry ice/acetone bath. The side arm containing the decanted solution was then cooled to −196 °C, and the apparatus was evacuated. The crystalline products were dried under dynamic vacuum at the appropriate temperature ($FXeONO_2$, −78 °C; $XeF_2 \cdot HNO_3$, −80 °C; $XeF_2 \cdot N_2O_4$, −10 °C) before the side arm containing the supernatant was heat-sealed off under vacuum at −196 °C.

(a) $FXeONO_2$. Sulfuryl chloride fluoride (ca. 1.5 mL) was distilled at −78 °C onto a mixture of $FXeONO_2$, XeF_2, and $[NO_2][AsF_6]$ (vide supra) contained in a T-shaped FEP reaction

---

(56) Gerken, M.; Dixon, D. A.; Schrobilgen, G. J. *Inorg. Chem.* **2000**, *39*, 4244–4255.

(57) Lehmann, J. F.; Dixon, D. A.; Schrobilgen, G. J. *Inorg. Chem.* **2001**, *40*, 3002–3017.

vessel. The reactor was pressurized with ca. 1 atm of dry nitrogen and warmed to −30 °C, resulting in dissolution of XeF_2 and $FXeONO_2$. The colorless solution was cooled to −35 °C inside the crystal growth apparatus, whereupon colorless plates formed over a period of 2−3 h. The temperature was lowered to −50 °C over a period of 3−4 h, allowing for more complete crystallization. A crystal having the dimensions 0.22 × 0.16 × 0.04 mm^3 was selected for low-temperature X-ray structure determination.

(b) $XeF_2 \cdot HNO_3$. Sulfuryl chloride fluoride (ca. 1.5 mL) was distilled at −196 °C onto a sample of solid $XeF_2 \cdot HNO_3$ contained in a T-shaped FEP reaction vessel, followed by warming to −30 °C to effect dissolution. After several minutes of intense agitation, the adduct dissolved to give a clear, colorless solution. The solution temperature was lowered to −40 °C, and after ca. 15 min clear, colorless plates began to grow on the walls of the reactor. Over the course of the ensuing 7 h, the temperature was lowered to −60 °C, providing a large quantity of crystalline material. A crystal having the dimensions 0.20 × 0.13 × 0.04 mm^3 was selected for low-temperature X-ray structure determination.

(c) $XeF_2 \cdot N_2O_4$. A solution of XeF_2 in liquid N_2O_4 was prepared by condensing N_2O_4 (ca. 1.5 mL) onto XeF_2 (ca. 150 mg) at −3 °C, followed by dissolution of XeF_2 at 10 °C. Crystal growth was initiated at 3 °C, yielding long needles of XeF_2. Upon cooling to −3 °C, plates began to form on the needles over the ensuing hour and continued to grow over the next 6 h, after which time the N_2O_4 supernatant was decanted at −3 °C. A plate having the dimensions 0.16 × 0.08 × 0.04 mm^3 was selected for low-temperature X-ray structure determination.

4.8.2. Collection and Reduction of X-ray Data. Crystals were mounted at −100 ± 3 °C as previously described.[56] Crystals of $FXeONO_2$ and $XeF_2 \cdot N_2O_4$ were centered on a P4 Siemens diffractometer equipped with a Siemens SMART 1K CCD charge-coupled device (CCD) area detector that used the program SMART[58] and a rotating anode using graphite-monochromated Mo Kα radiation ($\lambda = 0.71073$ Å). Diffraction data collection (−30 °C) consisted of a full ϕ-rotation at $\chi = 0°$ using 0.3° (1040 + 30) frames, followed by a series of short (80 frames) ω scans at various ϕ and χ settings to fill the gaps. The crystal-to-detector distance was 4.999 cm, and the data collection was carried out in a 512 × 512 pixel mode using 2 × 2 pixel binning. Processing of the raw data was completed using SAINT+,[59] which applied Lorentz and polarization corrections to three-dimensionally integrated diffraction spots. The program SADABS[60] was used for the scaling of diffraction data, the application of a decay correction, and an empirical absorption correction based on the intensity ratios of redundant reflections.

A crystal of $XeF_2 \cdot HNO_3$ was centered on a Bruker SMART APEX II diffractometer, equipped with an APEX II 4K CCD area detector, a three-axis goniometer controlled by the APEX2 Graphical User Interface (GUI) software,[61] and a sealed-tube X-ray source (Mo target) emitting Kα radiation ($\lambda = 0.71073$ Å) monochromated by a graphite crystal. Diffraction data collection (−160 °C) consisted of a full ϕ-rotation at a fixed $\chi = 54.74°$ with 0.36° (1010) frames, followed by a series of short (250 frames) ω scans at various ϕ settings to fill the gaps. The crystal-to-detector distance was 4.969 cm, and the data collection was carried out in a 512 × 512 pixel mode using 2 × 2 pixel binning. Processing of the raw data was completed using the APEX2 GUI software,[61] which applied Lorentz and polarization corrections to three-dimensionally integrated diffraction spots. The program SADABS[62] was used for the scaling of diffraction data, the application of a decay correction, and an empirical absorption correction based on the intensity ratios of redundant reflections.

4.8.3. Solution and Refinement of the Structures. The XPREP[63,64] program was used to confirm the unit cell dimensions and the crystal lattices. The solution was obtained by direct methods, which located the positions of the atoms defining the $FXeONO_2$ molecule and the $XeF_2 \cdot HNO_3$ and $XeF_2 \cdot N_2O_4$ adducts. The structure of $FXeONO_2$ was solved as a racemic twin. The final refinements for all structures were obtained by introducing anisotropic thermal parameters and the recommended weightings for all of the atoms except hydrogen. The maximum electron densities in the final difference Fourier maps were located near the heavy atoms. All calculations were performed using the SHELXTL package[63,64] for the structure determinations and solution refinements and for the molecular graphics.

4.9. Computational Methods. Quantum-chemical calculations were carried out using MP2, PBE1PBE, and B3LYP methods, as implemented in the program Gaussian 09,[65] for the geometry optimizations and vibrational frequencies and intensities, and the program Gaussian 03,[66] for the NBO analyses. The standard all-electron aug-cc-pVTZ basis set, as implemented in the Gaussian program, was utilized for all elements except Xe, for which the semi-relativistic large core (RLC) pseudopotential basis set, aug-cc-pVTZ-PP, was used.[67] The combined use of aug-cc-pVTZ and aug-cc-pVTZ-PP basis sets is indicated by aug-cc-pVTZ(-PP). The program GaussView[68] was used to visualize the vibrational displacements that form the basis of the vibrational mode descriptions given in Tables 4, 6, and 7 and Tables S5−S8, S10, S12, and S14 in the Supporting Information. Natural bond orbital analyses were carried out using B3LYP and MP2 densities with the NBO program (version 3.1).[69−71]

Acknowledgment. This work is dedicated to Prof. Dr. Boris Žemva on the occasion of his 70th birthday. We thank the Natural Sciences and Engineering Research Council of Canada for support in the form of a Discovery Grant (G.J.S.) and the award of postgraduate scholarships (M.D.M.), and the Ontario Graduate Scholarship in Science and Technology and the McMaster Internal Prestige "Ontario Graduate Fellowships" Programs for support (D.S.B.), and the computational resources provided by SHARCNET (Shared Hierarchical Academic Research Computing Network, www.sharcnet.ca).

Supporting Information Available: Calculated geometrical parameters for $FXeON(O)F^+$ and $FXeFNO_2^+$ (Table S1) and their calculated geometries and relative zero-point energies

---

(58) *SMART*, release 5.054; Siemens Energy and Automation Inc.: Madison, WI, 1999.

(59) *SAINT*, release 6.01; Siemens Energy and Automation Inc.: Madison, WI, 1999.

(60) Sheldrick, G. M. *SADABS* (Siemens Area Detector Absorption Corrections), version 2.03; Siemens Analytical X-ray Instruments Inc.: Madison, WI, 1999.

(61) *APEX2*, release 2.0-2; Bruker AXS Inc.: Madison, WI, 2005.

(62) Sheldrick, G. M. *SADABS* (Siemens Area Detector Absorption Corrections), version 2.10; Siemens Analytical X-ray Instruments, Inc.: Madison, WI, 2004.

(63) Sheldrick, G. M. *SHELXTL*, release 5.1; Siemens Analytical X-ray Instruments, Inc.: Madison, WI, 1998.

(64) Sheldrick, G. M. *SHELXTL*, release 6.14; Siemens Analytical X-ray Instruments, Inc.: Madison, WI, 2000−2003.

(65) Frisch, M. J.; et al. *Gaussian 09*, revision A.02; Gaussian, Inc.: Wallingford, CT, 2009.

(66) Frisch, M. J.; et al. *Gaussian 03*, revision D.01; Gaussian, Inc.: Wallingford, CT, 2004.

(67) Basis sets were obtained from the Extensible Computational Chemistry Environment Basis set Database, version 2/25/04, as developed and distributed by the Molecular Science Computing Facility, Environmental and Molecular Science Laboratory, which is part of the Pacific Northwest Laboratory, P.O. Box 999, Richland, WA 99352.

(68) Dennington, R. I.; Keith, T.; Millam, J. M.; Eppinnett, K.; Hovell, W. L.; Gilliland, R. *GaussView*, version 3.07 ed.; Semichem, Inc.: Shawnee Mission, KS, 2003.

(69) Reed, A. E.; Weinstock, R. B.; Weinhold, F. *J. Chem. Phys.* **1985**, *83*, 735–746.

(70) Reed, A. E.; Curtiss, L. A.; Weinhold, F. *Chem. Rev.* **1988**, *88*, 899–926.

(71) Glendening, E. D.; Reed, A. E.; Carpenter, J. E.; Weinhold, F.; *NBO*, version 3.1; Gaussian, Inc.: Pittsburgh, PA, 1990.

(Figure S1); Raman spectra of $FXeONO_2$ recorded at −160 °C after 5 h at −50 °C and after 5 days −78 °C (Figure S2); gas-phase $\Delta H°$, $\Delta G°$, $\Delta H_{195.15}$, and $\Delta G_{195.15}$ for the synthesis and decomposition reactions of $FXeONO_2$, $Xe(ONO_2)_2$, $XeONO_2^+$, and N_2O_6 (Table S2); experimental and calculated geometrical parameters for $FXeONO_2$, $XeF_2{\cdot}HNO_3$, and $XeF_2{\cdot}N_2O_4$ at PBE1PBE and MP2 levels of theory using the aug-cc-pVTZ(PP) basis set (Table S3); experimental and calculated geometrical parameters and NBO analyses for $FXeONO_2$, $BrONO_2$, and $ClONO_2$ (Table S4); packing diagram for $XeF_2{\cdot}HNO_3$ (Figure S3); calculated vibrational frequencies and intensities for the ^{16}O- and ^{15}N-enriched isotopomers of $FXeONO_2$ (Table S5); experimental and calculated vibrational frequencies and intensities for $XeF_2{\cdot}HNO_3$ at the PBE1PBE and MP2 levels of theory (Table S6) and for $XeF_2{\cdot}N_2O_4$ (Table S7); experimental and calculated vibrational frequencies, geometrical parameters and bond orders, valencies, and NPA charges from NBO analyses for XeF_2 (Table S8); experimental and calculated geometrical parameters (Table S9) and vibrational frequencies for HNO_3 (Table S10); calculated geometrical parameters (Table S11) and vibrational frequencies for N_2O_4 (Table S12); factor-group analyses for $FXe^{16}ON^{16}O_2$ and $FXe^{16}ON^{16}O^{18}O$ (Table S13); calculated vibrational frequencies for $N^{16}O_2^+$, $^{18}ON^{16}O^+$, and $N^{18}O_2^+$ (Table S14); factor-group analysis for $XeF_2{\cdot}HNO_3$ (Table S15); calculated geometrical parameters for $Xe(ONO_2)_2$ (Table S16); calculated geometry for $Xe(ONO_2)_2$ (Figure S4); NBO analyses for $FXeONO_2$, $XeF_2{\cdot}HNO_3$, $XeF_2{\cdot}N_2O_4$, $Xe(ONO_2)_2$, HNO_3, and N_2O_4 (Table S17); solid-state thermochemistry of $[XeONO_2][AsF_6]$; correlation of ^{19}F and ^{129}Xe NMR parameters and group electronegativities; detailed syntheses of natural abundance and ^{15}N-enriched NO_2F; complete refs 65 and 66; and X-ray crystallographic files in CIF format for the structure determinations of $FXeONO_2$, $XeF_2{\cdot}HNO_3$, and $XeF_2{\cdot}N_2O_4$. This material is available free of charge via the Internet at http://pubs.acs.org.

JA105618W